Large-eddy simulation and Reynolds-averaged Navier-Stokes modeling of a reacting Rayleigh-Taylor mixing layer in a spherical geometry

Brandon E. Morgan, Britton J. Olson, Wolfgang J. Black, and Jacob A. McFarland

Large-eddy simulation and Reynolds-averaged Navier-Stokes modeling of a reacting Rayleigh-Taylor mixing layer in a spherical geometry

Brandon E. Morgan and Britton J. Olson
Lawrence Livermore National Laboratory
Livermore, California 94550

Wolfgang J. Black and Jacob A. McFarland
Department of Mechanical and Aerospace Engineering,
University of Missouri
Columbia, Missouri 65211

Tenth-order compact difference code *Miranda* is used to perform large-eddy simulation (LES) of a hydrogen gas/plastic mixing layer in a spherical geometry. Once the mixing layer has achieved self-similar growth, it is heated to 1 keV, and the second-order arbitrary Lagrangian/Eulerian (ALE) code *Ares* is used to simulate mixing layer evolution as it undergoes thermonuclear (TN) burn. Both premixed (in which deuterium and tritium are initially present in the gas) and non-premixed (in which deuterium is initially present only in the plastic) variants are considered at Atwood numbers 0.05 and 0.50. The impact of turbulent mixing on mean TN reaction rate is examined, and a four-equation k-L-a-V Reynolds-averaged Navier Stokes (RANS) model is presented. The k-L-a-V model, which represents an extension of the k-L-a model [B. Morgan and M. Wickett, "Three-equation model for the self-similar growth of Rayleigh-Taylor and Richtmyer-Meshkov instabilities," *Phys. Rev. E* **91**, 043002 (2015)] by the addition of a transport equation for the scalar mass fraction variance, is then applied in one-dimensional simulations of the reacting mixing layer under consideration. Excellent agreement is obtained between LES and RANS in total TN neutron production when fluctuations in reaction cross-section can be neglected.

I. INTRODUCTION

When fluids of differing densities are subject to an acceleration that is opposite in direction to the mean density gradient, the conditions exist for Rayleigh-Taylor (RT) instability [1, 2]. In certain cases, such as in supernovae [3, 4] and in inertial confinement fusion (ICF) applications [5–8], RT instability can occur in the presence of additional convergence effects as a result of spherical or cylindrical geometries[9, 10]. These geometrical effects, often referred to generally as Bell-Plesset (BP) effects, can affect RT linear-phase growth rates and may lead to an earlier onset of mode coupling [11–13].

In the indirect-drive approach to ICF, laser energy is absorbed by a high-Z enclosure known as a *hohlraum*. The hohlraum then emits x-rays, which are used to drive ablation and implode a hydrogen fuel capsule surrounded by the hohlraum [7]. RT instability at the hydrogen-ablator interface is known to contribute to the degradation of target performance in experiments conducted at the National Ignition Facility (NIF) [14]. For this reason, a series of experiments have been conducted at NIF to study mixing due to hydrodynamic instability in which tritium (T) gas is initially separated from a deuterated plastic (CD) layer [15]. By analyzing the resulting neutron spectra, researchers were able to identify the signature of the DT reaction ($D + T \rightarrow {}^4He + n^0$) in order to obtain an experimental measurement directly tied to the amount of instability-induced mixing [16]. In simu-

lations of these so-called *CD Symcap* experiments [16] as well in the development and analysis of many other ICF targets [17–20], it has become common practice to utilize Reynolds-averaged Navier-Stokes (RANS) modeling approaches to simulate turbulent mixing of the fuel and ablator materials. Until recently, however, the turbulent contribution to the average thermonuclear (TN) reaction rate has been neglected by common RANS approaches such as the k-L [21], k-L-a [22, 23], and BHR [24–27] models.

Since RANS remains a common tool for the design and assessment of ICF targets, the present work is concerned with developing and validating a RANS modeling approach for reacting, buoyancy-driven turbulent mixing. Whereas the *CD Symcap* experiments dealt with initally separated (i.e., *non-premixed*) reactants, ICF targets designed for ignition and gain typically utilize *premixed* DT fuel [7]. A RANS approach for reacting turbulence in ICF must therefore be general enough to handle both premixed and non-premixed reactants. Ristorcelli [28] has proposed an approach for closing the turbulent contribution to the average TN reaction rate using the density-specific-volume covariance, b, for binary, non-premixed reactants. While the Ristorcelli approach may potentially be useful in conjunction with a RANS model such as BHR [27], little validation work has yet been done, and the model's reliance on b would seem to suggest divergent behavior in the limit of zero Atwood number. In the present work, an alternative approach is presented

based on extending the *k-L-a* model [22, 23] with an additional transport equation for the mass fraction scalar variance, V.

Since detailed turbulence statistics are generally not available from ICF experiments, high-fidelity simulation represents an attractive alternative to provide baseline data for RANS model validation. Previous three-dimensional simulations of RT [4, 29, 30] and Richtmyer-Meshkov (RM) [31–33] instability in a convergent or spherical geometry have generally been limited to simulation of an octant or sector of a sphere or cylinder in order to conserve computational resources. Unfortunately, such an approach imposes artificial symmetries at sector boundaries which can affect turbulence statistics in the neighborhood of these symmetry planes. A number of high-fidelity simulations of reacting ICF targets have additionally been performed [34–39]; however, in the case of these previous ICF simulations, the focus has generally been on the impact of large-scale symmetry perturbations and, as a result, data such as mean TN reaction rates have not been widely reported. In the present work, high-fidelity large-eddy simulation (LES) is performed of a reacting RT mixing layer in a full 4π, spherical geometry. Through manipulation of the LES initial conditions, it is possible to collect data at different Atwood numbers in both premixed and non-premixed configurations.

In present simulations, the computational mixing layer is allowed to develop until it reaches a self-similar state, as defined by previous work for a planar RT mixing layer [40]. Once the mixing layer has reached self-similarity, indicating that a steady-state magnitude of scalar variance has been achieved, the mixing layer is heated to 1 keV, and TN burn is initiated. Both premixed and non-premixed configurations are considered. In the premixed configuration, both deuterium and tritium are initially present together in the light gas material, and a CH plastic is taken as the heavy gas material. In the non-premixed configuration, only tritium is initially present in the light gas material, and a deuterated CD plastic is taken as the heavy gas material. For both configurations, simulations are performed at Atwood numbers 0.05 and 0.50 by varying the density of the heavy material. From these simulations, a time history of the mass-weighted average temperature is obtained. In order to compare directly with RANS, in which turbulent fluctuations of the reaction cross-section are neglected (as discussed in greater detail in Section III), a secondary set of large-eddy simulations are then run in which spatial variation in reaction cross-section is artificially eliminated by imposing a spatially uniform, time-varying temperature profile equal to the average temperature obtained from the preliminary set of simulations. These simulations are then compared with one-dimensional (1D) RANS simulations of the same reacting RT mixing layer with both the *k-L-a* and the new *k-L-a-V* models. It is shown that when turbulent fluctuations in the reaction cross section can be neglected, the *k-L-a-V* model is able to accurately

capture the turbulent contribution to the mean TN reaction rate.

The remainder of this paper is laid out as follows. First, in Sections II A through II D, a description is given of the governing equations as well as the *Miranda* and *Ares* codes used in the present work. In Section II E, the *k-L-a-V* model is presented, and similarity analysis is used to determine constraints on model coefficients necessary to reproduce the expected mixedness of an RT mixing layer. Next, in Sections II F and II G, detailed descriptions are given of the computational setup of the spherical mixing layer problem for LES and RANS. Results are presented in Section III for premixed and non-premixed configurations, and comparisons are made between LES and RANS data. Finally, in Section IV conclusions are drawn, and recommendations are made concerning the direction of future research.

II. NUMERICAL MODELS

A. Hydrodynamics equations

The governing equations are the compressible Navier-Stokes equations for a multicomponent, reacting flow:

$$\frac{\partial \rho}{\partial t} + \frac{\partial (\rho u_i)}{\partial x_i} = 0 \,, \tag{1}$$

$$\frac{\partial (\rho Y_k)}{\partial t} + \frac{\partial (\rho Y_k u_i)}{\partial x_i} = -\frac{\partial J_{k,i}}{\partial x_i} + \dot{r}_k \,, \tag{2}$$

$$\frac{\partial (\rho u_j)}{\partial t} + \frac{\partial (\rho u_i u_j)}{\partial x_i} = -\frac{\partial p}{\partial x_j} + \frac{\partial \tau_{ij}}{\partial x_i} + \rho g_j \,, \tag{3}$$

$$\frac{\partial E}{\partial t} + \frac{\partial [(E+p)\, u_i]}{\partial x_i} = \frac{\partial (\tau_{ij} u_i)}{\partial x_j} - \frac{\partial q_i}{\partial x_i} + \rho g_i u_i + \dot{Q} \,. \tag{4}$$

In Eqs. (1) through (4), ρ is density, t is time, u_i is the velocity vector, x_i is the spatial coordinate vector, Y_k is the mass fraction of species k, $J_{k,i}$ is the diffusive mass flux of species k, $\dot{r}_k$ is the reaction rate of species k, p is pressure, τ_{ij} is the viscous stress tensor, g_j is a gravitational body force vector, E is the total energy, q_i is the heat flux vector, and $\dot{Q}$ is the heat source term. The diffusive mass flux is given in terms of effective binary diffusion coefficients D_k as

$$J_{k,i} = -\rho \left(D_k \frac{\partial Y_k}{\partial x_i} - Y_k \sum_{j=1}^{N} D_j \frac{\partial Y_j}{\partial x_i} \right) \,, \tag{5}$$

for k=1, 2, . . . , N total species. The viscous stress tensor is given by

$$\tau_{ij} = 2\mu S_{ij} + \left(\beta - \frac{2}{3}\mu\right)\frac{\partial u_i}{\partial x_i}\delta_{ij}\,, \tag{6}$$

where μ is the shear viscosity, β is the bulk viscosity, δ_{ij} is the Kronecker delta, and S_{ij} is the strain rate tensor,

$$S_{ij} = \frac{1}{2}\left(\frac{\partial u_i}{\partial x_j} + \frac{\partial u_j}{\partial x_i}\right)\,. \tag{7}$$

The heat flux vector is given in terms of the thermal conductivity κ, the temperature T, and species enthalpy h_k,

$$q_i = -\kappa\frac{\partial T}{\partial x_i} + \sum_{k=1}^{N} h_k J_{k,i}\,. \tag{8}$$

Component temperature, enthalpy, and pressure are obtained through the equation-of-state (EOS) as a function of component partial density and specific internal energy. These relationships are given functionally as

$$p_k = P_{\mathrm{EOS}}\left(e_k, \rho_k\right)\,, \tag{9a}$$

$$T_k = T_{\mathrm{EOS}}\left(e_k, \rho_k\right)\,, \tag{9b}$$

$$h_k = H_{\mathrm{EOS}}\left(e_k, \rho_k\right)\,. \tag{9c}$$

Using an assumption of pressure and temperature equilibrium, an iterative process is used to solve for component volume fractions, v_k, which allows the determination of partial densities and energies according to

$$\rho_k = \frac{Y_k\rho}{v_k}\,, \tag{10}$$

and

$$e = \frac{E}{\rho} - \frac{1}{2}u_i u_i = \sum_{k=1}^{N} Y_k e_k\,. \tag{11}$$

Total pressure is then determined according to the mixture relationship

$$p = \sum_{k=1}^{N} v_k p_k\,. \tag{12}$$

TABLE I. Summary of AFLES terms in *Miranda*.

ψ^*	C_ψ	$f(U)$	ϕ
β^*	7.0×10^{-2}	ρ	$\frac{\partial u_i}{\partial x_i}$
μ^*	1.0×10^{-4}	$\frac{\rho}{\Delta}$	u_i
κ^*	1.0×10^{-3}	$\frac{\rho}{T\Delta_t}c_v$	T
D_k^*	1.0×10^{-2}	$\frac{1}{\Delta_t}$	Y_k

B. The *Miranda* code

The *Miranda* code solves the hydrodynamics equations presented in section II A with a tenth-order compact differencing scheme for spatial discretization and a fourth-order explicit Runge-Kutta scheme for temporal integration. It has been utilized extensively in previous studies of RT and RM mixing [40–47]. To model the subgrid scale (SGS) transfer of energy, Miranda utilizes an artificial fluid LES (AFLES) approach in which artificial transport terms are added to the fluid viscosity, the bulk viscosity, the thermal conductivity, and the molecular diffusivity [48, 49]. Equations (13a) through (13d) describe the formulation used in the present study where the subscript f denotes the fluid, or physical, contribution to the molecular transport property, and an asterisk superscript denotes the artificial contribution.

$$\mu = \mu_f + \mu^*\,, \tag{13a}$$

$$\beta = \beta_f + \beta^*\,, \tag{13b}$$

$$\kappa = \kappa_f + \kappa^*\,, \tag{13c}$$

$$D_k = D_{f,k} + D_k^*\,. \tag{13d}$$

In Eqs. (13a) through (13d), each artificial term assumes a general form given by

$$\psi^* = C_\psi\overline{f(U)G(\phi)\Delta^2}\,, \tag{14}$$

where the overbar notation indicates application of a truncated-Gaussian filter, and Δ is the local mesh spacing. $G(\phi)$ represents the application of an eighth-derivative operation such that for a scalar ϕ,

$$G(\phi) = \max\left(\left|\frac{\partial^8\phi}{\partial x^8}\Delta x^8\right|, \left|\frac{\partial^8\phi}{\partial y^8}\Delta y^8\right|, \left|\frac{\partial^8\phi}{\partial z^8}\Delta z^8\right|\right)\,, \tag{15}$$

and for a vector ϕ_i,

$$G(\phi_i) = \max\left(G\left(\phi_x\right), G\left(\phi_y\right), G\left(\phi_z\right)\right)\,. \tag{16}$$

Table I summarizes the formulation of the artificial fluid terms used in *Miranda*. In this table, c_v is the specific heat coefficient at constant volume, and Δ_t is the time step. Since the present study is focused on the high-Reynolds number regime in which viscous length scales are significantly smaller than energy-containing structures, the approach of Olson *et al.* [44] is adopted, and fluid contributions to molecular transport properties are neglected such that $\mu_f = \beta_f = \kappa_f = D_{f,k} = 0$.

C. Radiation diffusion equations

In the present work, coupling between radiation and hydrodynamics is treated with a Planckian non-equilibrium diffusion model. A single opacity, ω, is used to characterize both the energy absorbed from the radiation field and the energy contributed from the material to the radiation field via emission. The radiation energy E_r is then evolved according to

$$\frac{\partial E_r}{\partial t} = \frac{\partial}{\partial x_i}\left(\frac{c}{3\omega\rho}\frac{\partial E_r}{\partial x_i}\right) + c\omega\rho\left(a_r T_e^4 - E_r\right), \quad (17)$$

where c is the speed of light in a vacuum, T_e is the electron temperature, and a_r is the radiation constant which is given in terms of the Stefan-Boltzmann constant σ_{SB} by

$$a_r \equiv \frac{4}{c}\sigma_{\text{SB}}. \quad (18)$$

Electron and ion energies are allowed to evolve separately, with the ion energy given by Eq. (4) and the electron energy E_e given by,

$$\frac{\partial E_e}{\partial t} + \frac{\partial (E_e u_i)}{\partial x_i} = -\frac{\partial q_{e,i}}{\partial x_i} + \dot{Q}_e. \quad (19)$$

The electron heat flux vector $q_{e,i}$ is given in terms of the electron conductivity κ_e by

$$q_{e,i} = -\kappa_e \frac{\partial T_e}{\partial x_i}. \quad (20)$$

The ion and electron fields are then coupled to the radiation field through the source terms which are given by

$$\dot{Q}_e = \frac{\rho c_v K_{ie}}{\Delta_t}\left(T_i - T_e\right) + c\omega\rho\left(E_r - a_r T_e^4\right) + \dot{Q}_{TN,e}, \quad (21)$$

$$\dot{Q} = \frac{\rho c_v K_{ie}}{\Delta_t}\left(T_e - T_i\right) + \dot{Q}_{TN,i}. \quad (22)$$

TABLE II. Summary of TN reactions supported by *Ares*.

No.	reaction	Q_{TN} (MeV)
1	$D + D \rightarrow n^0 + {}^3\text{He}$	3.26
2	$D + D \rightarrow {}^1\text{H} + T$	4.02
3	$T + T \rightarrow n^0 + n^0 + {}^4\text{He}$	11.32
4	$D + T \rightarrow n^0 + {}^4\text{He}$	17.59
5	$D + {}^3\text{He} \rightarrow {}^1\text{H} + {}^4\text{He}$	18.35

In equations (21) and (22), K_{ie} is the ion-electron coupling coefficient, and T_i is the ion temperature. The specific heat, electron, and ion temperatures are determined from the EOS, and the radiation temperature is related to the radiation energy by

$$E_r = a_r T_r^4. \quad (23)$$

$\dot{Q}_{TN,e}$ and $\dot{Q}_{TN,i}$ in Eqs. (21) and (22) are source terms due to local deposition of energy from TN reactions, which will be discussed in more detail in the next section.

D. The *Ares* code

The *Ares* code solves the coupled radiation-hydrodynamics equations using an arbitrary Lagrangian/Eulerian (ALE) approach with a second-order remap [50]. Explicit time integration is accomplished with a second-order predictor-corrector scheme [51], and spatial differences are computed with a non-dissipative second-order finite element approach. A tensor artificial viscosity [52] is applied for the capturing of shocks and material discontinuities. Although *Ares* also boasts an adaptive mesh refinement (AMR) capability [53, 54], it is not utilized in the present study. *Ares* has been applied previously in studies of canonical RM instability in both planar [46] and cylindrical [55] configurations. It has also been utilized extensively in the simulation of ICF targets and experiments [14, 16, 20, 56–59].

In the present work, five TN reactions are computed by *Ares*, as summarized by Table II. In these reactions, products can be either neutrons, indicated by n^0, or charged particles. The rate of a given reaction with products γ and reactants α and β is given simply by

$$\dot{r}_{\gamma,\alpha\beta} = \langle\sigma v\rangle_{\alpha\beta} n_\alpha n_\beta \quad (24)$$

where $\langle\sigma v\rangle_{\alpha\beta}$ is the reaction cross-section, and n_α and n_β are the particle number densities. The reaction cross-section is interpolated using the TDFv2.3 library [60]. Additionally, each reaction has an average thermal energy, which is tabulated in Table II. Local deposition of this energy is assumed such that the average thermal

energy is removed from the ion energy field, and charged particle energy is deposited in the same volume with a split between the ion and electron energies according to the Corman-Spitzer model [61]. Neutrons are assumed to immediately escape the problem, and energy carried by neutron products is removed from the system. Thermal effects and the apportionment of average thermal energy amongst reactants is determined following the method by Warshaw [60]. Additionally, the ion-electron coupling coefficient K_{ie} is determined according to Brysk [62].

E. The k-L-a-V RANS model

The k-L-a-V model represents an extension of the k-L-a model [22, 23] by the addition of a transport equation for the variance of the mass fraction of species k, denoted by $V_k \equiv \widetilde{Y_k'' Y_k''}$. The model equations are derived from the compressible RANS equations for a multi-component, reacting gas mixture. In the present work, an overbar denotes Reynolds averaging, and a tilde denotes mass-weighted (Favre) averaging. An arbitrary scalar, f, is decomposed as

$$f = \overline{f} + f' = \widetilde{f} + f'' , \qquad (25)$$

where the Favre average is related to the Reynolds average through the density, ρ, according to

$$\widetilde{f} = \frac{\overline{\rho f}}{\overline{\rho}} . \qquad (26)$$

The Reynolds stress tensor, turbulence kinetic energy, mass-flux velocity vector, and density–specific-volume covariance are defined, respectively, by

$$\overline{\rho} R_{ij} \equiv -\overline{\rho u_i'' u_j''} , \qquad (27a)$$

$$\overline{\rho} k \equiv \frac{1}{2} \overline{\rho u_i'' u_i''} , \qquad (27b)$$

$$a_i \equiv -\overline{u_i''} , \qquad (27c)$$

$$b \equiv -\overline{\rho' \left(\frac{1}{\rho}\right)'} . \qquad (27d)$$

Notice that the convention used here is that the Reynolds stress is negated, in the style of Wilcox [63].

Equations (28)–(40) below summarize the k-L-a-V model, where L is the turbulence length scale and μ_t is the eddy viscosity. The model coefficients C_μ, C_a, C_b, C_B, C_D, C_{L1}, C_{L2}, C_{V1}, C_{V2}, N_a, N_e, N_k, N_L, N_V, N_Y, and C_{dev} are set through similarity analysis. The model equations are

$$\frac{D\overline{\rho}}{Dt} = -\overline{\rho} \frac{\partial \widetilde{u}_i}{\partial x_i} , \qquad (28)$$

$$\overline{\rho} \frac{D\widetilde{Y}_k}{Dt} = \frac{\partial}{\partial x_i}\left(\frac{\mu_t}{N_Y} \frac{\partial \widetilde{Y}_k}{\partial x_i}\right) + \overline{r}_k , \qquad (29)$$

$$\overline{\rho} \frac{D\widetilde{u}_j}{Dt} = \overline{\rho} g_j - \frac{\partial \overline{p}}{\partial x_j} + \frac{\partial}{\partial x_i}\left(\overline{\rho} R_{ij}\right) , \qquad (30)$$

$$\overline{\rho} \frac{D\widetilde{e}}{Dt} = -\overline{p} \frac{\partial \widetilde{u}_i}{\partial x_i} - a_i \frac{\partial \overline{p}}{\partial x_i} + C_D \frac{\overline{\rho}(2k)^{3/2}}{L} + \frac{\partial}{\partial x_i}\left(\frac{\mu_t}{N_e} \frac{\partial \widetilde{e}}{\partial x_i}\right) , \qquad (31)$$

$$\overline{\rho} \frac{Dk}{Dt} = \overline{\rho} R_{ij} \frac{\partial \widetilde{u}_i}{\partial x_j} + a_i \frac{\partial \overline{p}}{\partial x_i} - C_D \frac{\overline{\rho}(2k)^{3/2}}{L} + \frac{\partial}{\partial x_i}\left(\frac{\mu_t}{N_k} \frac{\partial k}{\partial x_i}\right) , \qquad (32)$$

$$\overline{\rho} \frac{DL}{Dt} = C_{L1} \overline{\rho} \sqrt{2k} + C_{L2} \overline{\rho} R_{ij} \frac{L}{k} \frac{\partial \widetilde{u}_i}{\partial x_j} + \frac{\partial}{\partial x_i}\left(\frac{\mu_t}{N_L} \frac{\partial L}{\partial x_i}\right) , \qquad (33)$$

$$\overline{\rho} \frac{Da_j}{Dt} = C_B^2 \hat{b} \frac{\partial \overline{p}}{\partial x_j} - C_a \overline{\rho} a_j \frac{\sqrt{2k}}{L} + R_{ij} \frac{\partial \overline{\rho}}{\partial x_i} + \frac{\partial}{\partial x_i}\left(\frac{\mu_t}{N_a} \frac{\partial a_j}{\partial x_i}\right) , \qquad (34)$$

$$\overline{\rho} \frac{DV_k}{Dt} = C_{V1} \mu_t \frac{\partial \widetilde{Y}_k}{\partial x_i} \frac{\partial \widetilde{Y}_k}{\partial x_i} - C_{V2} \overline{\rho} \frac{\sqrt{2k}}{L} V_k + \frac{\partial}{\partial x_i}\left(\frac{\mu_t}{N_V} \frac{\partial V_k}{\partial x_i}\right) , \qquad (35)$$

where

$$\frac{D}{Dt} \equiv \frac{\partial}{\partial t} + \widetilde{u}_i \frac{\partial}{\partial x_i} , \qquad (36)$$

$$\mu_t = C_\mu \overline{\rho} \sqrt{2k} L , \qquad (37)$$

$$\widetilde{S}_{ij} = \frac{1}{2}\left(\frac{\partial \widetilde{u}_i}{\partial x_j} + \frac{\partial \widetilde{u}_j}{\partial x_i}\right) - \frac{1}{3} \frac{\partial \widetilde{u}_k}{\partial x_k} \delta_{ij} , \qquad (38)$$

$$\overline{\rho} R_{ij} = C_{dev} 2\mu_t \widetilde{S}_{ij} - \frac{2}{3} \overline{\rho} k \delta_{ij} . \qquad (39)$$

For the special case of binary mixing, $V_1 = V_2 = V$, and Ristorcelli [28] derives the following expression which is utilized here to close b,

$$\hat{b} \equiv C_b b \approx C_b \left(\frac{r\overline{\rho}}{\rho_H} \right)^2 V . \qquad (40)$$

In Eq. (40), r is a constant factor that can be written in terms of the Atwood number, $A \equiv \frac{\rho_H - \rho_L}{\rho_H + \rho_L}$, or as a ratio of the heavy fluid density ρ_H to the light fluid density ρ_L,

$$r \equiv \frac{\rho_H}{\rho_L} - 1 = \frac{2A}{1-A} . \qquad (41)$$

Finally, to derive a closure for the average reaction rate, the expression $m_\alpha n_\alpha = \rho Y_\alpha$ is utilized to transform Eq. (24) to the following form in terms of the species molar mass m_α,

$$\dot{r}_{\gamma,\alpha\beta} = \frac{\langle \sigma v \rangle_{\alpha\beta} Y_\alpha Y_\beta \rho^2}{m_\alpha m_\beta} . \qquad (42)$$

Then, by applying a Reynolds decomposition and averaging, Eq. (42) is transformed into

$$\overline{\dot{r}_{\gamma,\alpha\beta}} = \frac{\langle \sigma v \rangle_{\alpha\beta} \widetilde{Y}_\alpha \widetilde{Y}_\beta \overline{\rho}^2}{m_\alpha m_\beta}$$
$$\left\{ 1 + \frac{\widetilde{Y_\alpha'' Y_\beta''}}{\widetilde{Y}_\alpha \widetilde{Y}_\beta} + \frac{\overline{\rho'\rho'}}{\overline{\rho}^2} + \frac{\overline{\rho'Y_\alpha''}}{\overline{\rho}\widetilde{Y}_\alpha} + \frac{\overline{\rho'Y_\beta''}}{\overline{\rho}\widetilde{Y}_\beta} + \text{h.o.t.} \right\} , \qquad (43)$$

where fluctuations of the cross-section have been neglected, and third- and fourth-order moments have been indicated by the abbreviation h.o.t. (high-order terms).

At this point, it is useful to notionally differentiate between *materials* and *reactants*. By convention, a reactant may be taken to be any species for which a mass fraction evolution equation is solved. To simplify the closure problem, however, it is useful to group reactants into heavy and light materials. For example, in the present problem D and T are considered reactants while more generally light gas and heavy plastic are considered materials. Thus, reactants may be initially premixed, as in a DT (light gas) material mixing with CH (heavy plastic) material, or non-premixed, as in T (light gas) material mixing with CD (heavy plastic) material. An assumption is then made that fluctuations of reactant mass fractions can be related to fluctuations of the containing material mass fraction. For instance, if reactant α is in the light material, then using Y_L to indicate the mass fraction of the light material,

$$\frac{Y_\alpha''}{\widetilde{Y}_\alpha} \approx \frac{Y_L''}{\widetilde{Y}_L}, \qquad (44)$$

or

$$Y_\alpha'' \approx Y_L'' \frac{\widetilde{Y}_\alpha}{\widetilde{Y}_L} . \qquad (45)$$

For binary mixing, V can be used to model the mass-fraction covariance term directly; however, further closure is required for the density variance and the density-mass-fraction covariance terms. To close these terms, an incompressible RT mixing layer is considered with a linear density profile given by

$$\rho = Y_H \Delta\rho + \rho_L = (1 - Y_L)\Delta\rho + \rho_L , \qquad (46)$$

where Y_H and Y_L indicate, respectively, the heavy material mass fraction and the light material mass fraction, and $\Delta\rho = \rho_H - \rho_L$. Using Eq. (46), it is then possible to write

$$\rho' = \rho - \overline{\rho} = \Delta\rho Y_H'' = -\Delta\rho Y_L'' . \qquad (47)$$

Substituting Eq. (47) into Eq. (43), it becomes possible to transform the density variance and the density-mass-fraction covariances into functions of the mass-fraction covariance. If one further assumes that $\overline{\rho} \approx (\rho_H + \rho_L)/2$, as is the case in the low-Atwood number limit, these terms assume an Atwood number dependence. The density variance is thus closed by,

$$\frac{\overline{\rho'\rho'}}{\overline{\rho}^2} = \frac{(\Delta\rho)^2}{\overline{\rho}^2} \widetilde{Y_\alpha'' Y_\alpha''} \approx 4A^2 \widetilde{Y_\alpha'' Y_\alpha''} . \qquad (48)$$

The density-mass-fraction covariance term is peculiar in that the sign of this term may depend on a reference material. That is by plugging Eq. (47) into Eq. (43), one can write either

$$\frac{\overline{\rho'Y_\alpha''}}{\overline{\rho}\widetilde{Y}_\alpha} = \frac{\Delta\rho}{\overline{\rho}} \frac{\widetilde{Y_\alpha'' Y_H''}}{\widetilde{Y}_\alpha} \approx 2A \frac{\widetilde{Y_\alpha'' Y_H''}}{\widetilde{Y}_\alpha} , \qquad (49a)$$

or

$$\frac{\overline{\rho'Y_\alpha''}}{\overline{\rho}\widetilde{Y}_\alpha} = -\frac{\Delta\rho}{\overline{\rho}} \frac{\widetilde{Y_\alpha'' Y_L''}}{\widetilde{Y}_\alpha} \approx -2A \frac{\widetilde{Y_\alpha'' Y_L''}}{\widetilde{Y}_\alpha} . \qquad (49b)$$

Utilizing Eq. (47), the density-mass-fraction covariance can then be closed in terms of a mass-fraction variance with a sign that depends on which material contains the reactant α. In other words,

$$\frac{\overline{\rho'Y_\alpha''}}{\overline{\rho}\widetilde{Y}_\alpha} \approx \begin{cases} 2A \frac{\widetilde{Y_H'' Y_H''}}{\widetilde{Y}_H}, & \alpha \text{ in heavy material} \\ -2A \frac{\widetilde{Y_L'' Y_L''}}{\widetilde{Y}_L}, & \alpha \text{ in light material} \end{cases} . \qquad (50)$$

TABLE III. Summary of k-L-a-V model coefficients and the experimental values that constrain them.

α_b	$\frac{E_K}{\Delta\text{PE}}$	n	Θ	C_μ	C_a	C_b	C_B	C_D	C_{L1}	C_{V1}	C_{V2}	N_a	N_e	N_k	N_L	N_V	N_Y
0.06	0.50	1.11	0.80	0.204	0.339	5.00	0.857	0.354	0.283	46.67	0.849	0.060	0.060	0.060	0.030	0.060	0.060

1. Premixed reactants

If both reactants are well-mixed and in the same material with material mass fraction $\widetilde{Y}$,

$$Y''_\alpha \approx Y'' \frac{\widetilde{Y_\alpha}}{\widetilde{Y}}, \qquad (51a)$$

and

$$Y''_\beta \approx Y'' \frac{\widetilde{Y_\beta}}{\widetilde{Y}}. \qquad (51b)$$

Thus, the average reaction rate can be written as a function of the material mass fraction and the scalar variance only.

$$\overline{\dot{r}_{\gamma,\alpha\beta}} \approx \frac{\langle\sigma v\rangle_{\alpha\beta}\widetilde{Y}^2\overline{\rho}^2}{m_\alpha m_\beta}\left\{1 + \frac{V}{\widetilde{Y}^2} + 4A^2V \pm 4A\frac{V}{\widetilde{Y}}\right\}. \quad (52)$$

Notice that the sign of the density-mass-fraction covariance closure depends on the material in which the reaction occurs for an RT mixing layer. If the reaction occurs in the light material, the covariance will be negative; conversely, if the reaction occurs in the heavy material, the density-mass-fraction covariance will be positive.

2. Non-premixed reactants

If both reactants are initially in separate materials, then one reactant must be present in the heavy material and the other present in the light material. Then, if it is assumed that reactant α is in material with material mass fraction $\widetilde{Y}$,

$$Y''_\alpha \approx Y'' \frac{\widetilde{Y_\alpha}}{\widetilde{Y}}, \qquad (53a)$$

and

$$Y''_\beta \approx -Y'' \frac{\widetilde{Y_\beta}}{1-\widetilde{Y}}, \qquad (53b)$$

where binary mixing has been invoked such that $Y''_H = -Y''_L$ and $\widetilde{Y}_H = 1 - \widetilde{Y}_L$. Plugging Eqs. (53) back into Eq. (43), the average reaction rate then takes on the following more complicated form,

$$\overline{\dot{r}_{\gamma,\alpha\beta}} \approx \frac{\langle\sigma v\rangle_{\alpha\beta}\widetilde{Y}\left(1-\widetilde{Y}\right)\overline{\rho}^2}{m_\alpha m_\beta}$$
$$\left\{1 - \frac{V}{\widetilde{Y}\left(1-\widetilde{Y}\right)} + 4A^2V \pm 2A\left(\frac{V}{\widetilde{Y}} - \frac{V}{1-\widetilde{Y}}\right)\right\}. \quad (54)$$

Again, the sign of the density-mass-fraction covariance closure depends on the material in which the reaction occurs.

Self-similarity analysis, the details of which are fully contained in Appendix A, is utilized to derive constraints on model coefficients in terms of the RT growth parameter α_b, the RT energetics ratio $E_K/\Delta PE$, the homogeneous isotropic turbulence (HIT) decay exponent n, and the mixedness of an RT mixing layer given by,

$$\Theta \equiv \frac{\int_{-\infty}^\infty \widetilde{Y_H Y_L}\mathrm{d}x}{\int_\infty^\infty \widetilde{Y}_H\widetilde{Y}_L\mathrm{d}x} = 1 - \frac{\int_\infty^\infty \widetilde{Y''_H Y''_H}\mathrm{d}x}{\int_\infty^\infty \widetilde{Y}_H\widetilde{Y}_L\mathrm{d}x} = 1 - \frac{\int_\infty^\infty V\mathrm{d}x}{\int_\infty^\infty \widetilde{Y}_H\widetilde{Y}_L\mathrm{d}x}. \quad (55)$$

Table III summarizes the complete set of model coefficients used as well as the experimental values used to constrain them.

F. LES problem setup and initial conditions

LES simulations are conducted on a square Cartesian mesh extending between $-2R_c$ and $2R_c$ in each dimension, where R_c indicates the initial radius of the material contact surface. Light hydrogen gas with a density of $\rho_L = 0.011683$ g/cm^3 is initialized nominally out to a radius of $R_c = 1$ cm. Heavy CH plastic with an arbitrary density of $\rho_H = \rho_L(1+A)/(1-A)$ is initialized for radius $r > R_c$. Two configurations are considered: a premixed configuration and a non-premixed configuration. In the premixed configuration, the light gas is assumed to consist of a 3:1 DT mixture by atom fraction, and the plastic consists of carbon and hydrogen in an atom ratio of 1.35:1. In the non-premixed configuration, the light gas consists entirely of tritium, and the hydrogen content of the plastic is replaced with deuterium. A constant radial gravitational acceleration is balanced by a hydrostatic radial pressure gradient such that the mixing layer remains nominally centered around $r = R_c$ at later time. Constant mesh spacing, Δ, is utilized in all dimensions,

TABLE IV. Summary of LES mesh parameters.

Mesh	h_0/R_c	N_x	N_y	N_z	Total pts.
A	0.200	144	144	144	2.99M
B	0.100	288	288	288	23.9M
C	0.050	576	576	576	191M
D	0.025	1152	1152	1152	1.53B

such that $N_x = N_y = N_z$, and non-penetration boundary conditions are specified at all problem boundaries. Table IV summarizes the four levels of grid refinement considered in the present study. The ratio h_0/R_c indicates the initial mixing layer width.

Spherical harmonic functions are used to specify an initial perturbation spectrum at the contact surface. Since the goal of the present work is to study mixing layer behavior in the limit of self-similarity, it is desirable to maximize the total number of mixing layer generations simulated. Therefore, the approach of Morgan *et al.* [40], is adopted in the present work, and the perturbation spectrum is specified as a function of the mesh resolution such that each successive level of mesh refinement is expected to allow for one additional generation of mixing layer evolution. The initial perturbation amplitude is given by

$$\delta\left(r\right) = \begin{cases} \frac{\delta_0}{2}\left[\cos\left(2\pi\frac{r-R_c}{h_0}\right)+1\right], & \left|r-R_c\right| < \frac{h_0}{2} \\ 0, & \text{otherwise} \end{cases} , \quad (56)$$

where $\delta_0 = h_0/10$. An initial perturbation function is then defined according to

$$\eta\left(r,\theta,\phi\right) = \sum_{l=l_{\min}}^{l_{\max}} \sum_{m=-l}^{l} \delta\left(r\right) P_l^m\left(\theta+\psi_{l,m}, \phi+\xi_{l,m}\right) , \quad (57)$$

where P_l^m is the spherical harmonic function of order l and degree m, and $\psi_{l,m}$ and $\xi_{l,m}$ are phase shifts drawn from uniformly distributed random numbers between 0 and π and between 0 and 2π, respectively. For the present work, only the finest harmonic mode admitted by the mesh is used such that $l_{\min} = l_{\max} = N_x/2$. The perturbed mass fraction field is then defined as

$$Y_H\left(r,\theta,\phi\right) = \frac{1}{2}\left[\tanh\left(\frac{r-R_c+\eta\left(r,\theta,\phi\right)}{4\Delta}\right)\right] . \quad (58)$$

Simulations are evolved in *Miranda* using an ideal gas EOS until the homogeneous mixing layer width h_{hom}, as defined by

$$h_{\mathrm{hom}} \equiv 4\int_0^\infty \overline{Y}_H\left(1-\overline{Y}_H\right)\mathrm{d}r , \quad (59)$$
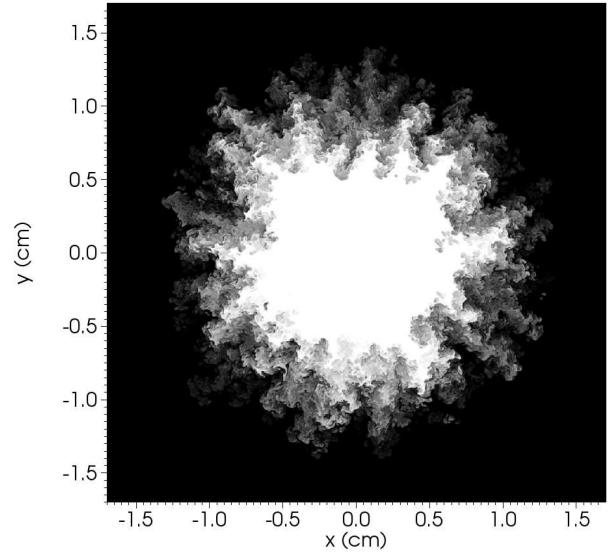

FIG. 1. Slice of Y_H contours at the $y = 0$ plane taken at $t = t_{\mathrm{burn}}$ for simulation on mesh D at $A = 0.05$. Contours are illustrated between $Y_H = 0$ (white) and $Y_H = 1$ (black).

exceeds $R_c/2$ (approximately 25% of the computational domain). Note that h_{hom} represents the thickness that would result if the entrained fluids were perfectly homogenized in θ and ϕ [42]. h_{hom} is a convenient measure for comparison with RANS calculations; however, when considering LES results in general the mixing layer half-width shall be taken as

$$h \equiv 4\int_0^\infty \overline{Y_H\left(1-Y_H\right)}\mathrm{d}r . \quad (60)$$

From Eq. (55), it is clear that h and h_{hom} are related according to

$$\Theta = \frac{h}{h_{\mathrm{hom}}} . \quad (61)$$

Once $h_{\mathrm{hom}} > R_c/2$, electron and ion temperatures are set to 1 keV everywhere, and the problem is continued with radiation diffusion and TN burn physics in the *Ares* code. Additionally, at this time which shall be denoted as t_{burn}, gravitational acceleration is turned off, boundary conditions are changed to extrapolation, and equations-of-state are changed to tabular Livermore EOS (LEOS) 1018 and LEOS 5350 for the gas and plastic, respectively [69, 70]. The simulation is then continued in *Ares* until the average electron temperature drops below 0.1 keV. In order to compare directly with RANS, a preliminary LES is run to obtain a realistic temperature time history. A secondary simulation is then carried out in which spatial variation in reaction cross-section is eliminated by imposing a spatially uniform, time-varying temperature profile obtained from the preliminary simulation.

In this way, large-eddy simulations are carried out in three parts. First, a hydrostatic RT mixing layer is evolved in a spherical geometry using the *Miranda* code until it reaches self-similarity and a steady-state value of the scalar mass fraction variance. During this stage of simulation, no reactions are occurring, and the problem is purely a hydrodynamic one. Then, once the mixing layer is fully developed, a second stage proceeds using the *Ares* code to compute the TN reactions with a fully coupled radiation-hydrodynamics treatment. During this second stage of simulation, turbulent fluctuations in temperature may exist, and an average temperature history is extracted. In the third and final stage, the *Ares* calculation is repeated with a spatially uniform, time-varying temperature profile set to the average temperature history extracted from the previous stage. By computing turbulence statistics obtained during the reacting stages of the calculation, it is possible to obtain validation data by which to evaluate the k-L-a-V RANS model and the average reaction rate closures given by Eqs. (52) and (54). Figure 1 illustrates an example mixing layer simulation at $t = t_{\text{burn}}$.

G. RANS problem setup and initial conditions

RANS simulations are conducted using the k-L-a-V model in *Ares*. Problems are solved in r-z geometry (with revolved symmetry about the z axis) on a quasi-1D wedge mesh of width $0.01°$ with 576 uniformly spaced computational zones extending out to a radius of $r = 2R_c$. A non-penetration boundary condition is assumed at $r = 2R_c$, and symmetry boundary conditions are assumed along the angular boundaries. Figure 2 illustrates the initial configuration of the mesh used.

Problems are set to match the LES as closely as possible, with the same material densities and compositions as described in the previous section. As in the LES problem, a constant radial acceleration is balanced by a hydrostatic radial pressure gradient such that during the non-reacting stage of the problem the mixing layer remains nominally centered about $r = R_c$. Turbulence quantities are initialized such that $L_{t=0} = 2.0 \times 10^{-6}$ cm and $k_{t=0} = 2.0 \times 10^{-12}$ cm^2/μs^2 in the two zones bordering the interface at $r = R_c$ and are zero everywhere else. This initialization procedure leads to an initial turbulence time scale, $L/\sqrt{2k}$, equal to 1 μs at the interface. Other turbulence quantities such as a_i and V_k are initially zero everywhere.

As in the LES problem, a non-reacting mixing layer is evolved with an ideal gas EOS until $h_{\text{hom}} > R_c/2$. After h_{hom} exceeds $R_c/2$, electron and ion temperatures are set to 1 keV everywhere, ideal gas equations-of-state are changed to tabular LEOS 1018 and 5350 for hot, dense matter [69, 70], and the problem is continued with radiation diffusion and TN burn physics active. Additionally, at t_{burn}, gravitational acceleration is turned off, and the $r = 2R_c$ boundary is changed to extrapolation. Tem-
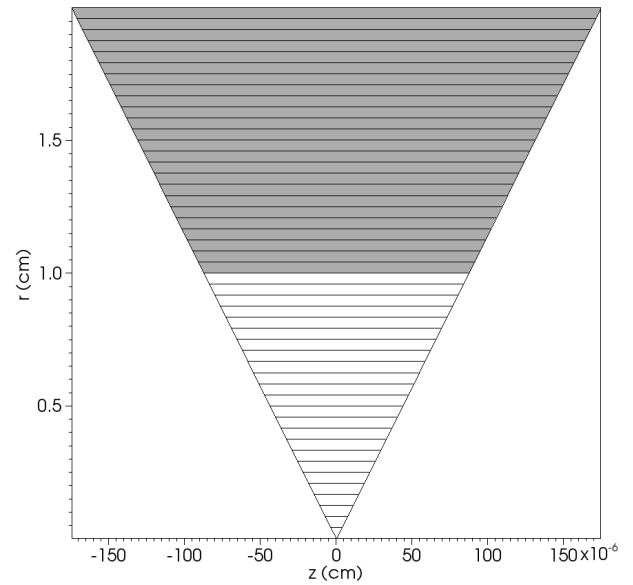

FIG. 2. Initial contours of Y_H plotted with the computational mesh (every 12th zone) used for RANS simulations. Contours are illustrated between $Y_H = 0$ (white) and $Y_H = 1$ (gray).
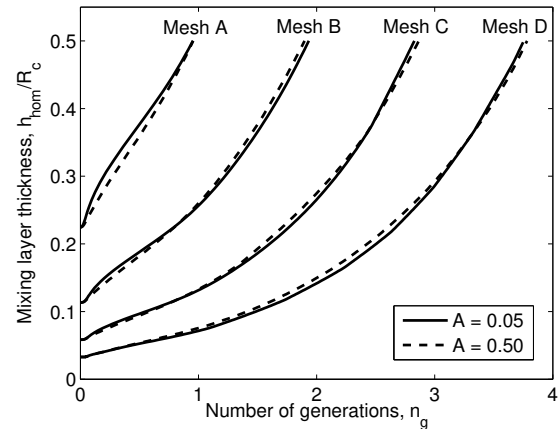

FIG. 3. Non-reacting mixing layer evolution as a function of generation number for four mesh resolutions at $A = 0.05$ and 0.50.

perature in RANS simulations is specified everywhere to equal the mass-weighted average temperature time history obtained from LES.

III. RESULTS AND DISCUSSION

A. Non-reacting mixing layer growth

As discussed by Morgan *et al.* [40], the generation number is a convenient way to non-dimensionalize time in mixing layer problems, and it represents the number of times the mixing layer has doubled in width,
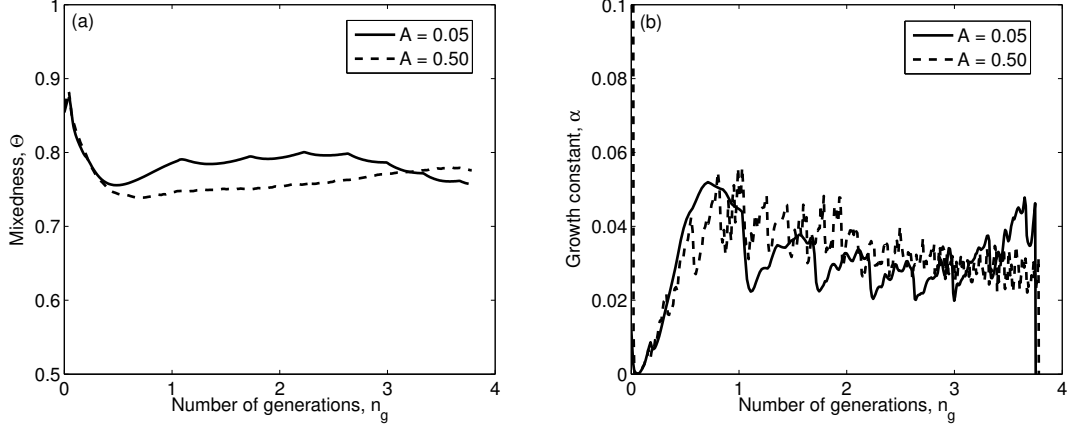
FIG. 4. Two measures of mixing layer development as a function of generation number on mesh D: (a) mixedness, Θ, and (b) growth constant, α, at $A = 0.05$ and 0.50.
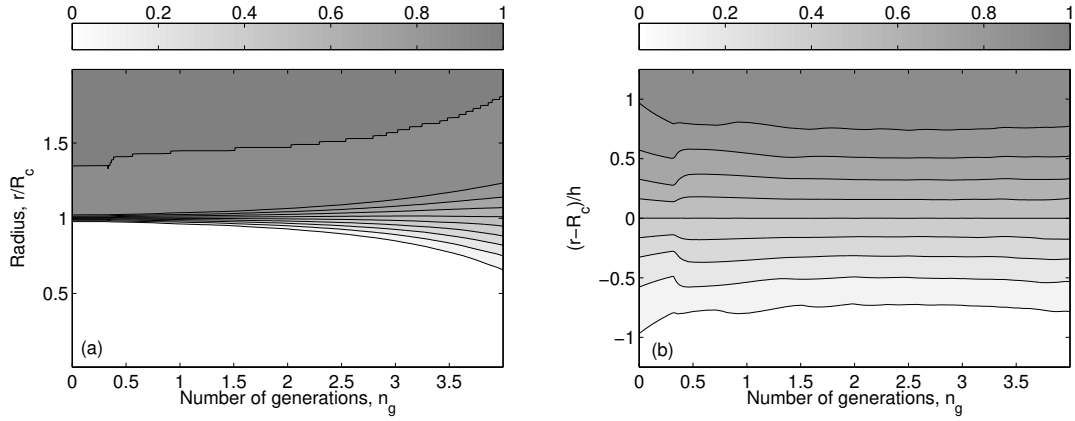

FIG. 5. Contours of radially averaged mass fraction as a function of time and space for simulation at $A = 0.05$ on mesh D: (a) $\widetilde{Y}_H$ vs. generation number and radial coordinate, r/R_c; (b) $\widetilde{Y}_H$ vs. generation number and self-similar radial coordinate $(r - R_c)/h$.

$$n_g(t) \equiv \log_2 \left(\frac{h(t)}{h(0)} \right) . \tag{62}$$

Figure 3 illustrates the mixing layer width h_{hom} as a function of generation number for obtained from LES for the four mesh resolutions considered at $A = 0.05$ and 0.50. As expected, each additional level of grid resolution allows for approximately one additional generation of mixing layer growth. Initial mixing layer widths are nearly equal to h_0, as previously given in Table IV, and t_{burn} occurs once $h_{\mathrm{hom}}/R_c > 0.50$.

Two additional indicators of mixing layer development are considered in Fig. 4. First, the mixedness Θ is plotted in Fig. 4a. For simulations at both $A = 0.05$ and 0.50, the mixedness is seen to approach a value of about 0.8, as expected. Notably, mixedness in the present results does not appear to drop significantly below 0.8 during the early-time evolution, as earlier simulations in a

planar geometry have often observed [40, 42, 71]. Since such a drop is generally indicative of the linear growth phase of dominant-mode perturbations, the relative suppression of such a feature in the present work is likely due to the combined impact of BP effects, which act to shorten the linear phase in a spherical geometry, and the single, highest-mode initial perturbation used in the present work. It might be expected, for instance, that an initial perturbation with more low-mode content would lead to a greater drop in initial mixedness.

Figure 4b additionally plots the RT growth constant α computed according to,

$$\alpha = \frac{h_t^2}{4 A g h} , \tag{63}$$

where h_t indicates the time derivative of h. Equation (63) has been derived alternately using self-similarity analysis [71] and an energy balance argument [41]. As illustrated
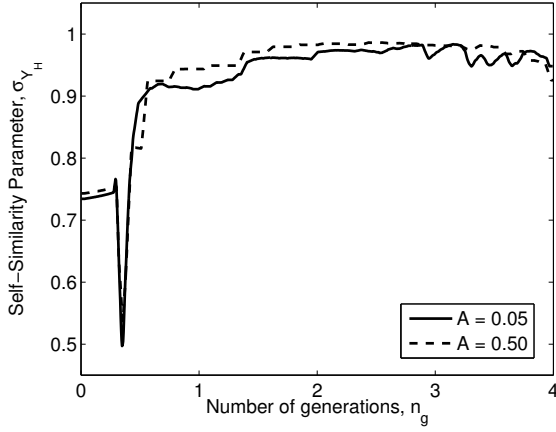
FIG. 6. Self-similarity of the heavy species mass fraction profile as a function of generation number for simulations on mesh D at $A = 0.05$ and 0.50.

FIG. 7. Spatial profile of photon mean free path from LES in the premixed configuration at $t_{\mathrm{burn}} + 0.0015\mu s$ on mesh D.

in Fig. 4b, by t_{burn} for both Atwood numbers, α appears to approach a value around 0.03.

For the purposes of comparing to RANS, which relies on assumptions of fully developed turbulence and self-similar growth, it is important that the LES results reach a state of self-similarity. To further quantify the degree to which the present LES results are self-similar, the approach of Morgan *et al.* [40] is adopted. Figure 5 plots contours of radially averaged mass fraction profiles as a function of generation number (i.e., time) and space. When the spatial coordinate is normalized by the mixing layer width, then as the mixing layer approaches self-similarity, contours should become horizontal. The degree to which the mass fraction contours demonstrate this kind of self-similar behavior is therefore quantified by the self-similarity metric,

$$\sigma_{Y_H}\left(n_g\right) \equiv 1 - \frac{\int_{-\infty}^{\infty}\left|\frac{\partial \widetilde{Y}_H}{\partial n_g}\right|\mathrm{d}\chi}{\int_{-\infty}^{\infty}\sqrt{\left(\frac{\partial \widetilde{Y}_H}{\partial n_g}\right)^2 + \left(\frac{\partial \widetilde{Y}_H}{\partial \chi}\right)^2}\mathrm{d}\chi}, \quad (64)$$

where $\chi \equiv (r - R_c)/h$ is used to indicate the self-simlar spatial coordinate.

Figure 6 plots the self-similarity metric defined by Eq. (64) for simulations at $A = 0.05$ and 0.50. In both cases, σ_{Y_H} is observed to decrease sharply during the first generation of mixing layer growth before rising again quite rapidly. Around $n_g \approx 2.5$, both cases reach a maximum value of $\sigma_{Y_H} \approx 0.98$. By t_{burn}, which occurs after approximately four generations of growth, both cases appear to be well within the self-similar regime.
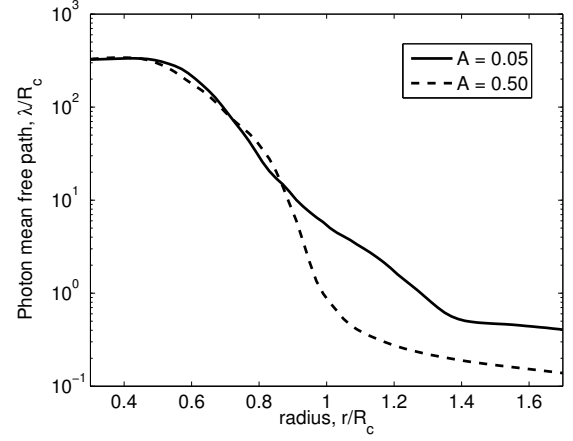
B. Burn with premixed reactants

1. LES Results

Attention is now turned to the second stage of simulations, in which the fully developed mixing layer simulations presented in the previous section are heated to 1 keV, and TN burn is allowed to proceed. A premixed configuration, in which D and T are initially well-mixed in the light fluid, is considered first. To provide a sense of how radiation behaves in this problem, Fig. 7 plots the average photon mean free path $\lambda \equiv \overline{(\rho \omega)^{-1}}$ across the mixing layer. In the light gas and across most of the mixing layer, λ is significantly greater than the mixing layer width. Although $\lambda/R_c < 1$ in the heavy fluid, the mixing layer itself is essentially transparent to the radiation field. As a result, E_r is nearly uniform in space throughout the problem evolution. Figure 8 illustrates the mass-weighted average temperature history of the evolving mixing layer in the first 30 ns after t_{burn} for both $A = 0.05$ and 0.50. In both cases, there is little difference between the ion and electron temperatures. A steep, nearly linear drop in electron and ion temperatures occurs over the first 4-8 ns in both cases, after which time the matter and radiation temperatures appear approximately to reach equilibrium. During this first 4-8 ns when the matter temperature is dropping sharply is when the majority of TN reactions occur in the present problem.

In order to better inform the RANS reaction rate closures discussed in Section II E, Fig. 9 plots the spatial profiles of contributions to the radially averaged DT reaction rate given by,
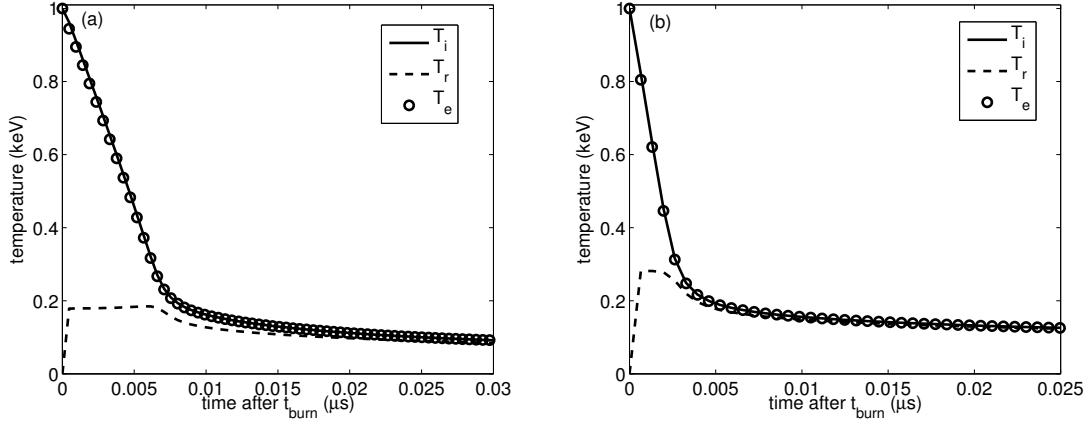
FIG. 8. Mass-weighted average temperature history of burning mixing layer LES in the premixed configuration on mesh D: (a) $A = 0.05$ and (b) $A = 0.50$.
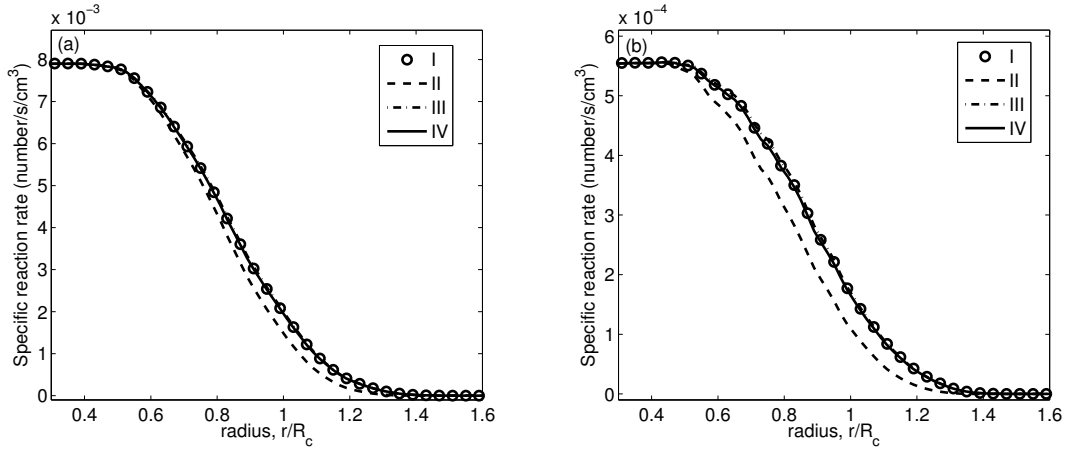

FIG. 9. Spatial profiles of radially averaged DT specific reaction rate from LES in the premixed configuration at $t_{\mathrm{burn}} + 0.0015$ μs on mesh D: (a) $A = 0.05$ and (b) $A = 0.50$. I. Radially averaged reaction rate. II. Mean contribution to reaction rate. III. Mean contribution plus scalar variance term. IV. Mean contribution plus all second moment terms. See Eq. (65) for mathematical definitions of curves.

FIG. 10. Spatial profiles of turbulent contributions to the average DT reaction rate from LES in the premixed configuration at $t_{\mathrm{burn}} + 0.0015$ μs on mesh D: (a) $A = 0.05$ and (b) $A = 0.50$. V. $\overline{\rho}^2 \widehat{Y_D'' \widetilde{Y_T''}}$. VI. $\widetilde{Y_D}\widetilde{Y_T}\overline{\rho'\rho'}$. VII. $\overline{\rho}\widetilde{Y_D}\overline{\rho'Y_T'}$. VIII. $\overline{\rho}\widetilde{Y_T}\overline{\rho'Y_D'}$.

$$\underbrace{\overline{\dot{r}_{\gamma,\alpha\beta}}}_{\text{I}} = \underbrace{\frac{\langle\sigma v\rangle_{\alpha\beta}\,\widetilde{Y}_\alpha\widetilde{Y}_\beta\overline{\rho}^2}{m_\alpha m_\beta}}_{\text{II}}\underbrace{\left(1 + \underbrace{\frac{\widetilde{Y''_\alpha Y''_\beta}}{\widetilde{Y}_\alpha\widetilde{Y}_\beta}}_{\text{V}} + \underbrace{\frac{\overline{\rho'\rho'}}{\overline{\rho}^2}}_{\text{VI}} + \underbrace{\frac{\overline{\rho'Y''_\alpha}}{\overline{\rho}\widetilde{Y}_\alpha}}_{\text{VII}} + \underbrace{\frac{\overline{\rho'Y''_\beta}}{\overline{\rho}\widetilde{Y}_\beta}}_{\text{VIII}} + \text{h.o.t.}\right)}_{\text{III}},}_{\text{IV}} \tag{65}$$

at a time 1.5 ns after t_{burn}. In this plot, curve I is the average reaction rate that must be modeled in RANS. Curve II is the mean contribution to the reaction rate that is modeled by k-L-a and other models which do not account for the additional contributions due to higher-order statistical moments. Curves III and IV represent closure models which account, respectively, for the contribution from the scalar variance only and for the contribution from all second moments. It is clear in Fig. 9 that the average reaction rate (curve I) is under-predicted by the mean contribution alone (curve II). Both curves III and IV appear to capture the average reaction rate quite well; although, for the $A = 0.50$ case, the reaction rate appears slightly over-predicted around $0.65 \lesssim r/R_c \lesssim 0.9$ when the density variance and covariance terms are ignored (term III). Of course, the density variance and density-mass-fraction covariance terms are expected to increase in magnitude with Atwood number; so, this is somewhat expected.

The relative magnitude of turbulence terms inside the parentheses in Eq. (65) is explored further in Fig. 10. In this figure, curve V is the spatial profile of the scalar variance contribution to the average DT reaction rate, and curve VI is the spatial profile of the density variance contribution to the average reaction rate. For the premixed configuration, the two density-mass-fraction covariance contributions are equivalent; so, the sum of these two terms is plotted together as a dotted line. Finally, the sum of all second moment contributions is plotted as a solid line. Since DT reactions are occurring in the light fluid, the density-mass-fraction covariance contribution is opposite in sign to the scalar variance and density variance contributions. Although the greatest single contributor to the reaction rate is the scalar variance term, the sum of all second moments is, therefore, somewhat less than the scalar variance contribution alone. As a result, if the covariance terms are neglected in a RANS model, the total reaction rate would be over-predicted, particularly at higher Atwood number. Although the density variance and density-mass-fraction covariance contributions are small at low Atwood number, as illustrated in Fig. 10b, these terms increase in relative magnitude at higher Atwood number, a finding which is consistent with the proposed closure model given by Eq. (52).

2. Comparison with RANS

Although the k-L-a-V RANS model development has relied on an assumption of constant reaction cross-section, as illustrated in Fig. 11, the present problem as developed thus far unfortunately has significant spatial temperature variance, which leads to equally significant spatial variance in cross-section. Figure 11a plots spatial profiles from LES of the standard deviation in temperature normalized by mean temperature, while Fig. 11b plots spatial profiles of the standard deviation in DT reaction cross-section, normalized by the mean cross-section. From this plot, it is clear that as much as 17% difference in cross-section exists within one standard deviation across the mixing layer, suggesting that the assumption of constant reaction cross-section is a poor one for the present problem. Therefore, to make direct comparisons with RANS, a second set of LES calculations is carried out in which the spatial variation in cross-section is artificially eliminated by specifying a uniform spatial temperature profile equal to the mass-weighted average temperature histories illustrated previously in Fig. 8.

Figure 12 illustrates representative mass fraction and scalar variance profiles from both LES and RANS simulations at $A = 0.05$ at t_{burn}. Although these profiles represent the end-state of the non-reacting phase of both simulations, the profiles illustrated in Fig. 12 also represent the initial conditions for the burn phase. In this regard, reasonable agreement is achieved between the RANS and LES in terms of profile shape and the peak magnitude of mass fraction variance.

The results illustrated in Fig. 13 represent the main diagnostic by which the k-L-a-V model is evaluated. In this figure, the total neutron production as a function of time is plotted for both LES and RANS simulations at $A = 0.05$ and 0.50. Three RANS simulations are compared against LES: k-L-a results with no modification to the mean reaction rate; k-L-a-V results with only the scalar variance contribution to the reaction rate, indicated as "k-L-a-V (without Atwood terms)"; and k-L-a-V results with reaction rate contributions from all second moments, indicated as "k-L-a-V (with Atwood terms)." For cases at both $A = 0.05$ and 0.50, it is clear that the k-L-a results under-predict the total neutron production by approximately 10-15%. While the density variance and density-mass-fraction covariance terms appear fairly negligible in the $A = 0.05$ case, as illustrated in Fig. 13b, if these terms are neglected at $A = 0.50$, the result is an over-prediction by almost the same amount. However,
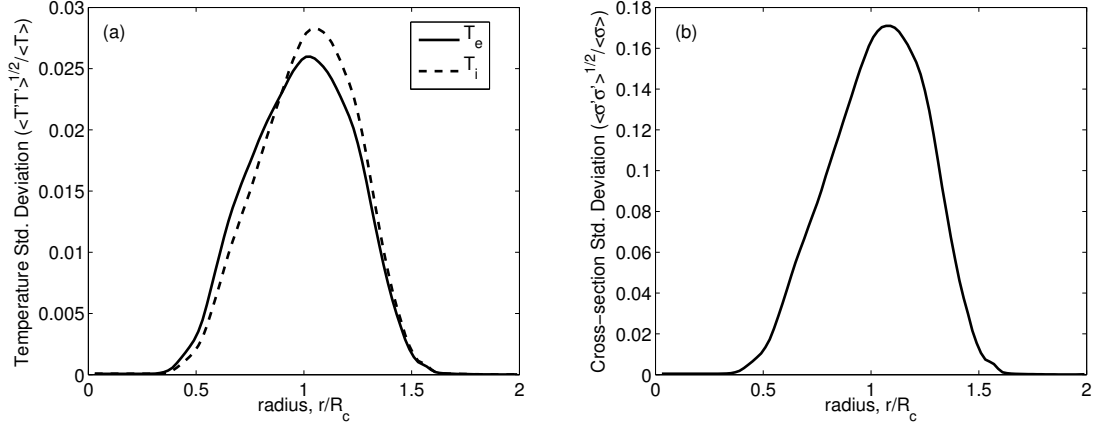
FIG. 11. Spatial profiles of normalized standard deviation of the form $\sqrt{\widetilde{f''f''}}/\widetilde{f}$ for (a) temperature and (b) DT reaction cross-section from LES in the premixed configuration at $t_{\mathrm{burn}} + 0.0015$ μs on mesh D.
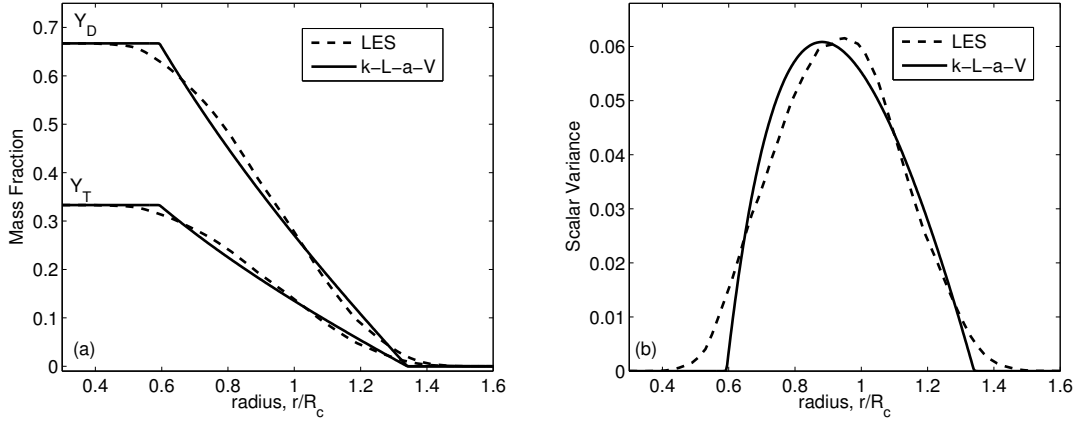

FIG. 12. Comparison of spatial profiles between LES (mesh D) and RANS in the premixed configuration at t_{burn} for $A = 0.05$: (a) mass fraction profiles, $\widetilde{Y}$, and (b) scalar variance profile, $\widetilde{Y''Y''}$.
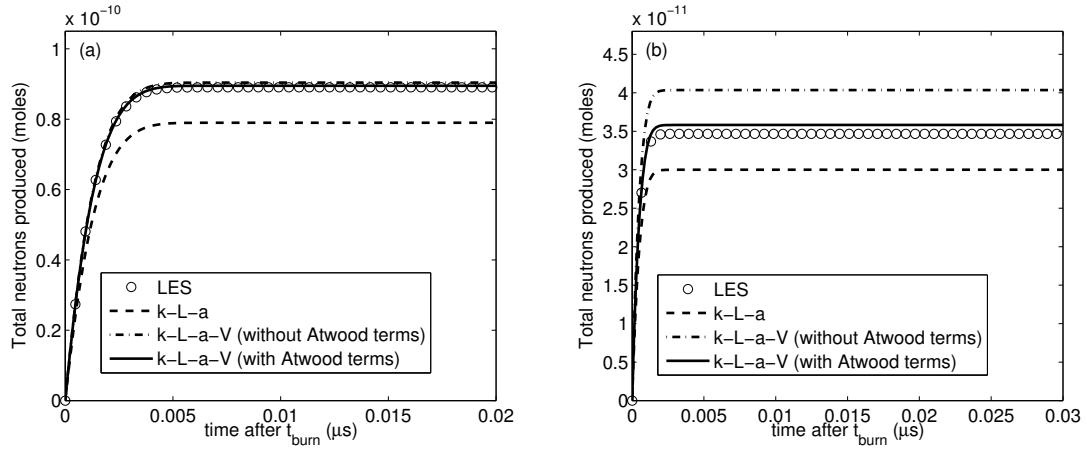

FIG. 13. Comparison of total neutron production as a function of time for LES (mesh D) and RANS in the premixed configuration: (a) $A = 0.05$ and (b) $A = 0.50$.

when all second moment contributions are modeled as given by Eq. (52), the k-L-a-V model predicts total neutron production to within 1% for the $A = 0.05$ case and to within 3% for the $A = 0.50$ case.

C. Burn with non-premixed reactants

1. LES Results

In the non-premixed configuration, T in the light gas is initially separated from D in the heavy plastic material. Although the code is capable of solving for all TN reactions listed in Table II, for the non-premixed configuration, DD and TT reactions are disabled to focus exclusively on the non-premixed DT reaction rate. Figure 14 plots the mass-weighted temperature evolution in the first 10ns after t_{burn}. Compared to the premixed configuration, there is slightly greater divergence between the ion and electron temperatures, and equilibration with the radiation temperature occurs over a shorter time period; however, the overall temperature history is qualitatively quite similar. The matter temperature decreases nearly linearly over a period of 2-4 ns, during which time most of the DT reactions occur, before slowly equilibrating with the radiation temperature.

Figure 15 plots spatial profiles of contributions to the average DT reaction rate, as previously defined by Eq. (65). In the non-premixed configuration, DT reactions only occur in the mixing layer region, and reaction rate profiles go to zero outside of the mixing layer. Additionally in the non-premixed configuration, the average contribution to the reaction rate (curve I) is observed to over-predict, rather than under-predict, the average reaction rate. This observation is consistent with the anticipated sign of the scalar variance contribution predicted by the closure model given by Eq. (54). Although there appears to be a slight under-prediction of the average reaction rate at $A = 0.50$ when the density-variance and density-mass-fraction covariance contributions are neglected (curve III), the difference between curves III and IV is quite small, particularly at $A = 0.05$ in Fig. 15a.

Individual terms within the parentheses in Eq. (65) are again explored in Fig. 16. In contrast to the premixed configuration in which the density-mass-fraction covariance terms are equal, in the non-premixed case, the two covariance terms are opposite in sign and are plotted separately in Fig. 16. At $A = 0.05$, the covariance terms act to nearly cancel each other, and the density variance is negligible in comparison to the scalar variance contribution; thus, at low Atwood number, the scalar variance accounts for nearly all of the turbulent contribution to reaction rate. At $A = 0.50$, the density variance is a more significant term, and the density-mass-fraction covariance terms do not cancel each other as closely.

2. Comparison with RANS

Figure 17 plots normalized standard deviations of temperature and DT cross-section for the non-premixed case. Compared to the premixed configuration (Fig. 11), standard deviations of both temperature and cross-section in the non-premixed configuration (Fig. 17) are significantly greater. In particular, the standard deviation of DT cross-section peaks at over 45% of the average for the non-premixed case. Such a high value again emphasizes that an assumption of constant cross-section is particularly poor for the non-premixed case, in which DT reactions occur only within the turbulent mixing layer. By contrast, in the premixed case, a significant fraction of DT reactions occur within the laminar core, where the assumption of a constant cross-section is more reasonable. Therefore, as done previously, a second set of LES calculations is carried out in which the spatial variation in cross-section is artificially eliminated by specifying a uniform spatial temperature profile equal to the mass-weighted average temperature histories illustrated in Fig. 14.

Mass fraction and scalar variance profiles at time t_{burn}, as illustrated in Fig. 18, again demonstrate that LES and RANS are in reasonable agreement for the initial conditions to the burn phase of simulations. As illustrated in Fig. 18a, in the non-premixed configuration, D and T are only present together within the turbulent mixing layer. Although the magnitude of the scalar variance in the mixing layer is about the same as in the premixed configuration, in general, the non-premixed configuration is more sensitive to turbulent fluctuations since reactions do not occur outside of the mixing layer.

Total neutron production as a function of time is plotted in Fig. 19 for both LES and RANS simulations at $A = 0.05$ and 0.50. Again, three sets of RANS results are compared against LES. In the non-premixed configuration, the k-L-a model over-predicts total neutron production by between 35% and 40% for both the $A = 0.05$ and 0.50 cases. This error is reduced to about 2.7% for the $A = 0.05$ case and to 5.5% for the $A = 0.50$ case, however, with the k-L-a-V model. As expected, inclusion of the density variance and density-mass-fraction covariance closures appears to have little impact in the lower Atwood number case; although, their inclusion in the $A = 0.50$ case modestly improves agreement with LES. This result is consistent with earlier observations in Fig. 16, in which the density-mass-fraction covariance terms were found to be opposite in sign with contributions to the average reaction rate that nearly cancel each other.

IV. SUMMARY AND CONCLUSIONS

In the present work, LES of a reacting RT mixing layer in a spherical geometry has been performed in order to obtain high-fidelity data on the impact of turbulent mixing on the average reaction rate. Four levels of mesh re-
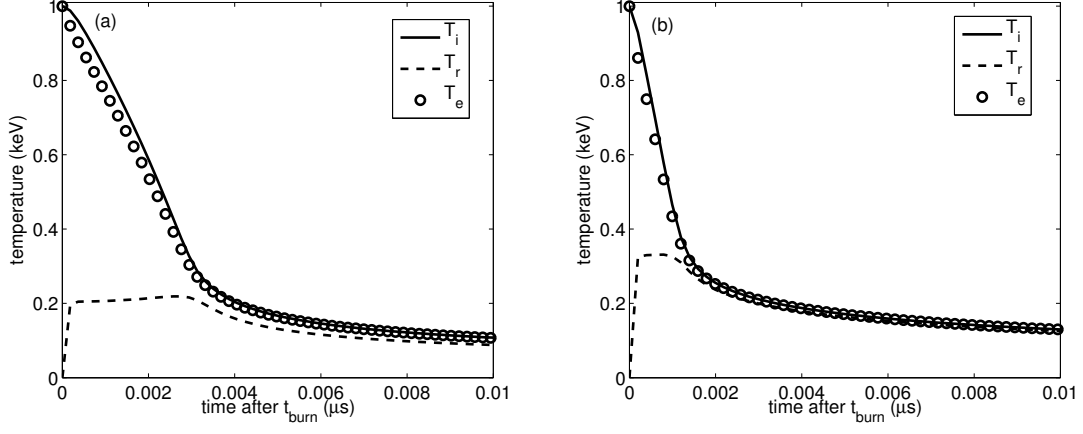
FIG. 14. Mass-weighted average temperature history of burning mixing layer LES in the non-premixed configuration on mesh D: (a) $A = 0.05$ and (b) $A = 0.50$.
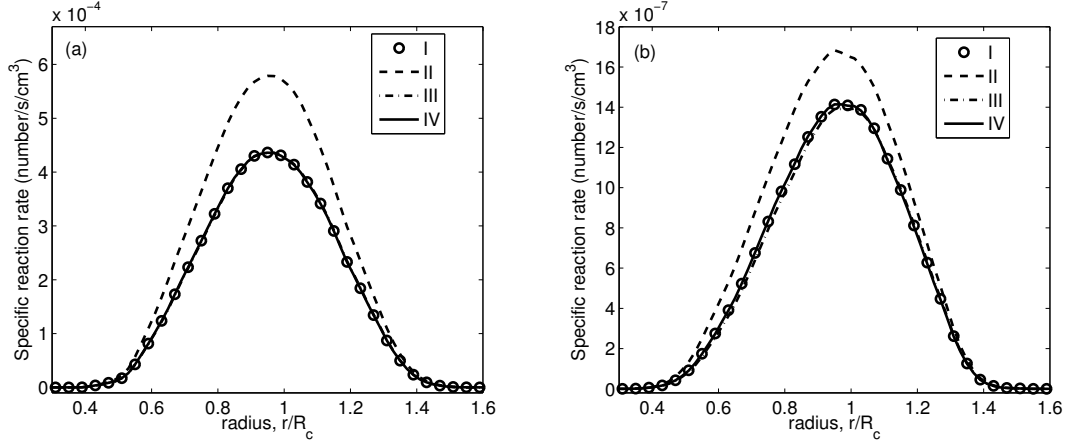

FIG. 15. Spatial profiles of radially averaged DT specific reaction rate from LES in the non-premixed configuration at $t_{\text{burn}} + 0.0015\ \mu s$ on mesh D: (a) $A = 0.05$ and (b) $A = 0.50$. I. Radially averaged reaction rate. II. Mean contribution to reaction rate. III. Mean contribution plus scalar variance term. IV. Mean contribution plus all second moment terms. See Eq. (65) for mathematical definitions of curves.

FIG. 16. Spatial profiles of turbulent contributions to the average DT reaction rate from LES in the non-premixed configuration at $t_{\text{burn}} + 0.0015\ \mu s$ on mesh D: (a) $A = 0.05$ and (b) $A = 0.50$. V. $\overline{\rho}^2 \widetilde{Y_D'' Y_T''}$. VI. $\widetilde{Y}_D \widetilde{Y}_T \overline{\rho' \rho'}$. VII. $\overline{\rho} \widetilde{Y}_D \overline{\rho' Y_T'}$. VIII. $\overline{\rho} \widetilde{Y}_T \overline{\rho' Y_D'}$.
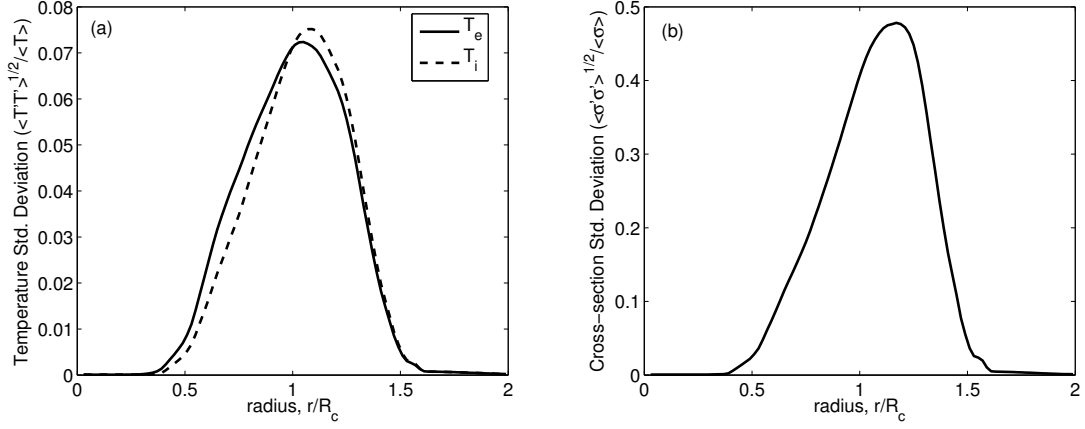
FIG. 17. Spatial profiles of normalized standard deviation of the form $\sqrt{\widetilde{f''f''}}/\widetilde{f}$ for (a) temperature and (b) DT reaction cross-section from LES in the non-premixed configuration at $t_{\mathrm{burn}} + 0.0015$ μs on mesh D.
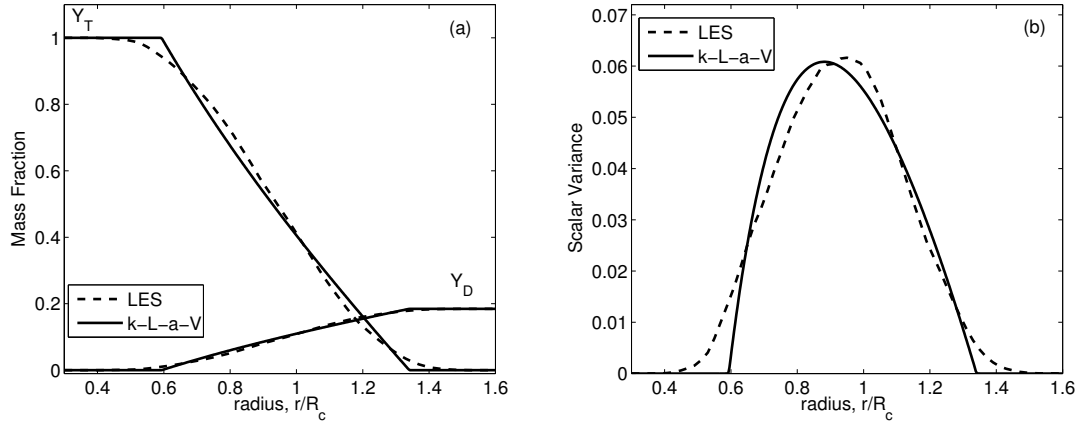

FIG. 18. Comparison of spatial profiles between LES (mesh D) and RANS in the non-premixed configuration at t_{burn} for $A = 0.05$: (a) mass fraction profiles, $\widetilde{Y}$, and (b) scalar variance profile, $\widetilde{Y''Y''}$.
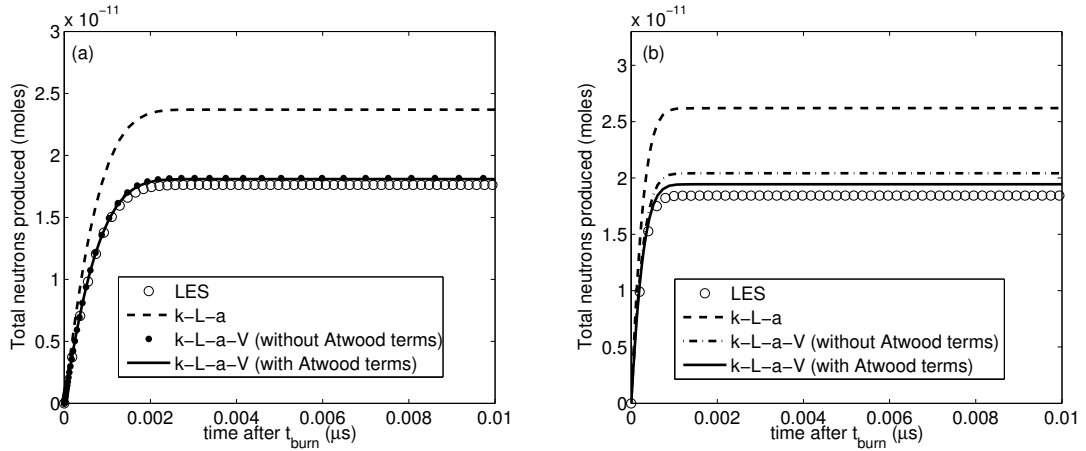

FIG. 19. Comparison of total neutron production as a function of time for LES (mesh D) and RANS in the non-premixed configuration: (a) $A = 0.05$ and (b) $A = 0.50$.

finement were considered, and the highest-resolution simulations were shown to reach a self-similar state, achieving a steady-state mixedness, $\Theta \approx 0.8$, and a steady-state growth rate, $\alpha \approx 0.03$.

After reaching self-similarity, simulations were then set to 1 keV to initiate TN burn. Both premixed and non-premixed configurations were considered at low (0.05) and moderate (0.50) Atwood numbers. Using data from the LES results, average reaction rate profiles were extracted and compared against potential second-moment turbulence closures. At low Atwood number, density variance and density-mass-fraction covariance contributions to the average reaction rate were found to be fairly negligible, and a reasonable closure of the reaction rate could be made with the scalar variance contribution alone. However, at $A = 0.50$, these terms became increasingly significant and could not be neglected. In both premixed and non-premixed configurations, the assumption of a constant reaction cross-section was found to be a poor approximation due to turbulent variations in temperature. To enable comparisons with RANS, a second set of simulations were then carried out in which the spatial variation in temperature was artificially eliminated by specifying a uniform temperature history.

LES results with specified temperature history were then compared with 1D RANS simulations using the k-L-a model [22, 23] and the newly proposed k-L-a-V model, which represents an extension of the k-L-a model by the addition of a transport model for scalar mass fraction variance. The k-L-a-V model, which was presented in Section II E, has been constrained through similarity analysis to reproduce the mixedness of a self-similar RT mixing layer in the limit of low Atwood number and includes proposed closure for the average reaction rate to include contribution from second-moment turbulence effects. When applied to simulation of the reacting RT mixing layer in a converging geometry, the k-L-a-V model was demonstrated to agree quite closely with LES in total neutron production, resulting in a reduction in error over the k-L-a model by about 12% in the premixed configuration and as much as 35% in the non-premixed configuration.

Of course, more work remains to be done. Most importantly, in the present work, the impact of turbulent fluctuations in the reaction cross-section have been neglected. A more complete model should account for density and mass fraction correlations with the fluctuating cross-section and model them appropriately. Therefore, the most immediate direction of future research should focus on developing appropriate closures for these terms. The spherical RT mixing layer considered in the present work is very much a manufactured problem. In reality, turbulence in ICF targets may be dominated by three-dimensional, low-mode asymmetries, and by viscous dissipation effects [36]. Additionally, representative Atwood numbers of realistic ICF targets are in general much greater than those considered in the present work. Further work should therefore be done to obtain high-

fidelity reaction rate data from simulation of more realistic ICF configurations. As the present work has shown, when turbulent fluctuations in reaction cross-section can be neglected, the k-L-a-V model is able to match LES very closely. Application of the model to the simulation of a more realistic ICF target for which high-fidelity simulation and/or experimental data exists would therefore represent a more rigorous test of the k-L-a-V model's usefulness in engineering applications.

Appendix A: Self-similarity analysis of the k-L-a-V model

Previous work [22, 23] has shown that a set of model coefficients can be derived for the k-L-a model which satisfy an ansatz of self-similar RT growth in the limit of low Atwood number. When self-similarity constraints are satisfied, the k-L-a model has been previously shown to reproduce experimentally observable parameters, such as RT and RM growth rates, that are used to constrain model coefficients. In a manner similar to the approach of Schilling and Mueschke [64], the k-L-a-V model differs from the k-L-a model only by the addition of the scalar variance transport equation, Eq. (35), and in the closure for b given in Eq. (40). Thus, similarity analysis for the k-L-a-V model follows identically the analysis for the k-L-a model [22] with additional consideration of the scalar variance equation and only minor difference in analysis of the a equation.

To begin, a change of variable is introduced in terms of the mixing layer half-width, $h(t)$. Let $\chi \equiv x/h$. It is assumed that k, L, and V are separable in space and time such that $k(\chi, t) = K_0(t)f(\chi)$, $L(\chi, t) = L_0(t)\sqrt{f(\chi)}$, and $V(\chi, t) = V_0(t)f(\chi)$ with $f(\chi) = 1 - \chi^2$. A linear mass fraction profile is assumed such that

$$\widetilde{Y}_H(\chi) = \frac{1}{2}(1 - \chi) , \qquad (A1a)$$

$$\widetilde{Y}_L(\chi) = \frac{1}{2}(1 + \chi) . \qquad (A1b)$$

Substituting into Eqs. (A1) into Eq. (55) allows one to derive the following simple relationship,

$$\Theta = 1 - 4V_0 \,. \tag{A2}$$

From prior work [40, 42], Θ is expected to approach a value of about 0.8 for a fully developed mixing layer. For a 1D RT mixing layer in the limit of low Atwood number, Eq. (35) reduces to

$$\overline{\rho}\frac{DV}{Dt} = C_{V1}\mu_t \left(\frac{\partial \widetilde{Y}}{\partial x}\right)^2 - C_{V2}\overline{\rho}\frac{\sqrt{2k}}{L}V_\alpha + \frac{\partial}{\partial x}\left(\frac{\mu_t}{N_V}\frac{\partial V}{\partial x}\right). \tag{A3}$$

Substituting into Eq. (A3) and utilizing the incompressibility assumption to cancel factors of density leads to

$$\frac{D}{Dt}\left(V_0 f\right) = C_{V1}C_\mu L_0 \sqrt{2K_0}\left(-\frac{1}{2h}\right)^2 f$$
$$- C_{V2}\frac{\sqrt{2K_0}}{L_0}V_0 f + \frac{\partial}{\partial x}\left[\frac{C_\mu L_0 f \sqrt{2K_0}}{N_V}\frac{\partial}{\partial x}\left(V_0 f\right)\right]. \tag{A4}$$

According to the similarity ansatz, the turbulence length scale is assumed to grow self-similarly such that $L_0 = \beta h$. From prior self-similarity analysis of the L equation [22, 23],

$$\beta = \sqrt{\frac{C_{L1}N_L}{2C_\mu}}\,, \tag{A5}$$

and

$$\frac{\partial L_0}{\partial t} = \frac{C_L}{2}\sqrt{2K_0}\,. \tag{A6}$$

Recognizing from Eq. (A2) that $\partial V_0/\partial t = 0$ in the self-similar regime, after some algebra and substitution of Eqs. (A5) and (A6), Eq. (A4) can be rearranged to give

$$\left[C_{L1}V_0 + \frac{C_{V1}C_{L1}N_L}{8} - C_{V2}V_0 - \frac{3C_{L1}N_L}{N_V}V_0\right]\chi^2$$
$$- \left[\frac{C_{V1}C_{L1}N_L}{8} - C_{V2}V_0 - \frac{C_{L1}N_L}{N_V}V_0\right] = 0\,. \tag{A7}$$

To ensure that both the χ^2 terms and the constant terms in Eq. (A7) go to zero simultaneously requires

$$N_V = 2N_L\,. \tag{A8}$$

Substituting Eq. (A8) back into Eq. (A7) reduces both sets of terms in brackets to

$$\frac{C_{V1}C_{L1}N_L}{8} - C_{V2}V_0 - \frac{C_{L1}}{2}V_0 = 0\,, \tag{A9}$$

which can be rearranged to solve for the following constraint on C_{V1} in terms of Θ,

$$C_{V1} = \frac{2C_{V2} + C_{L1}}{C_{L1}N_L}\left(1 - \Theta\right) \tag{A10}$$

To derive a constraint on the scalar variance dissipation constant C_{V2}, consider the decay of HIT. In the absence of mean velocity and pressure gradients, Eqs. (32), (33), and (35) reduce to

$$\frac{dk}{dt} = -C_D \frac{(2k)^{3/2}}{L}\,, \tag{A11a}$$

$$\frac{dL}{dt} = C_{L1}\sqrt{2k}\,, \tag{A11b}$$

$$\frac{dV}{dt} = -C_{V2}\frac{\sqrt{2k}}{L}V\,. \tag{A11c}$$

These equations are solved in terms of a reference time t_0, a turbulence decay constant n, and a scalar decay constant m.

$$k = K_0 \left(1 + \frac{t}{t_0}\right)^{-n}\,, \tag{A12a}$$

$$L = L_0 \left(1 + \frac{t}{t_0}\right)^{1-n/2}\,, \tag{A12b}$$

$$V = V_0 \left(1 + \frac{t}{t_0}\right)^{-m}\,. \tag{A12c}$$

Substituting Eqs. (A12a) and (A12b) into Eqs. (A11a) and (A11b) gives

$$n = \frac{2C_D}{C_{L1} + C_D}\,. \tag{A13}$$

Then, substituting Eq. (A13) along with Eqs. (A12a) through (A12c) back into Eq. (A11c) leads to

$$C_{V2} = m\left(C_{L1} + C_D\right)\,. \tag{A14}$$

Equation (A14) is general for any choice of the scalar decay constant m. While there is some uncertainty about a universal value of m, Sutton [65] suggests the following relationship between the velocity decay exponent n and the scalar decay exponent m,

$$m = \frac{1}{2}\left(6 - 3n\right) \tag{A15}$$

Substituting Eqs. (A15) and (A13) back into Eq. (A14) gives,

$$C_{V2} = 3C_{L1} \qquad (A16)$$

Applying the low-Atwood-number assumption that $\overline{\rho} \approx (\rho_H + \rho_L)/2$ to Eq. (40), one derives the self-similar profile for $\hat{b}$,

$$\hat{b} = C_b \frac{4A^2}{1 - 2A^2 + A^4} V_0 f \qquad (A17)$$

The remaining similarity analysis follows the same process previously described in some detail in Refs. [22] and [23]. From this analysis, it follows that the diffusion coefficients must all be related by

$$N_Y = N_e = N_k = N_a = N_V = 2N_L . \qquad (A18)$$

The buoyancy production coefficient, C_B, is constrained by the RT bubble growth parameter, α_b, according to

$$C_B = \frac{4\,\alpha_b \left(1 + 2\frac{C_D}{C_{L1}}\right)}{\sqrt{\frac{C_\mu\,C_{L1}}{N_k}}} . \qquad (A19)$$

The ratio $C_\mu C_{L1}/N_k$ is constrained by the RT growth parameter and the ratio of liberated kinetic energy, E_K, to the change in potential energy, ΔPE, according to

$$\frac{C_\mu\,C_{L1}}{N_k} = 8\,\alpha_b \frac{\Delta\text{PE}}{E_K} . \qquad (A20)$$

The a dissipation coefficient, C_a, is constrained according to

$$C_a = C_D + \frac{\sqrt{\frac{C_{L1}\,N_k}{C_\mu}}}{6\,C_B} - \frac{C_{L1}}{4} . \qquad (A21)$$

Finally, for the reduced a equation to be consistent with the reduced k equation, the scaling coefficient C_b must satisfy

$$C_b = \frac{1}{4V_0} = \frac{1}{1 - \Theta} . \qquad (A22)$$

Since there is no shear in a 1D RT mixing layer, the coefficients C_{L2} and C_{dev} can be neglected for the present purposes. When shear is a concern, a proper treatment for these coefficients has been derived in the context of the two-length-scale k-L-a model [23]. As discussed by Morgan *et al.* [23], however, when there is no shear the single length scale model is equivalent to the two-length-scale model.

Equations (A10), (A14), (A16), and (A18)-(A22) thus represent 12 constraints on the 14 model coefficients C_μ, C_a, C_b, C_B, C_D, C_{L1}, C_{V1}, C_{V2}, N_a, N_e, N_k, N_L, N_V, and N_Y. C_μ and C_D are chosen to be consistent with the original k-L-a model [22] such that $C_\mu\sqrt{2} = 0.288$ and $C_D 2^{3/2} = 1$. Similarly, the same set of experimental values as for the k-L-a model are used to set the RT growth parameter $\alpha_b = 0.06$ [66, 67], the RT energetics ratio $E_K/\Delta PE = 0.5$ [67, 68], and the HIT decay exponent $n = 1.11$. As mentioned earlier, $\Theta = 0.8$ is taken for the RT mixedness parameter [40, 42].

Figures 20 and 21 illustrate application of the k-L-a-V model to simulation of a planar 1D RT mixing layer at $A = 0.05$. Problem setup and initialization is the same as described by Morgan and Wickett [22], using the k-L-a-V model as implemented in *Ares*. As shown in Fig. 20, the steady-state scalar variance and b profiles predicted by k-L-a-V matches very closely the quadratic profiles that were used to derive the similarity constraints. Although the RANS model is incapable by construction of capturing the complex turbulence transition process, which the LES data exhibits during the first 4.5 generations of growth, as illustrated by Fig. 21 the desired mixedness is recovered exactly in the steady state with the k-L-a-V model.
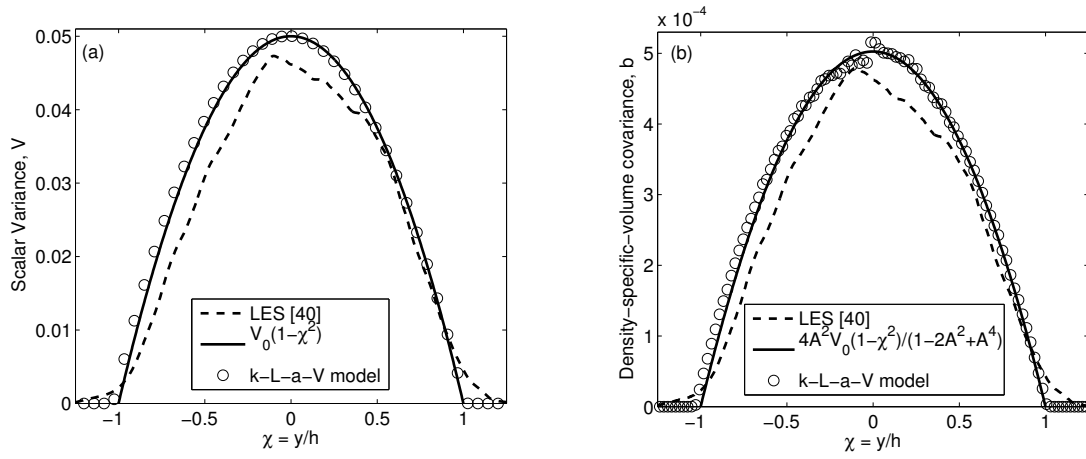
FIG. 20. The k-L-a-V model applied to simulation of a planar 1D RT mixing layer at $A = 0.05$: (a) steady-state scalar variance profile and (b) steady-state b profile compared with LES [40] and with similarity solution.
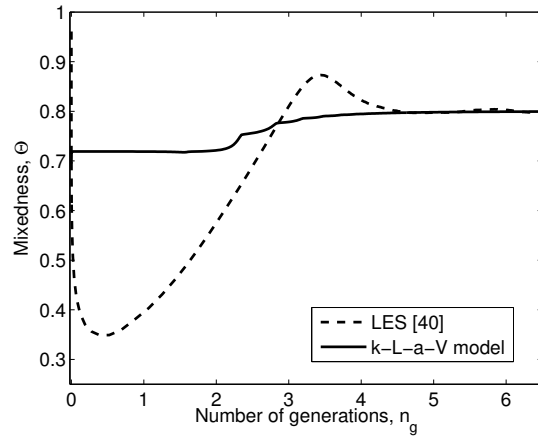
FIG. 21. The k-L-a-V model applied to simulation of a planar 1D RT mixing layer at $A = 0.05$: mixedness as a function of generation number compared with LES [40].

[1] Lord Rayleigh, "Investigation of the character of the equilibrium of an incompressible heavy fluid of variable density," Proc. R. Math. Soc. **14**, 170–177 (1883).

[2] G. I. Taylor, "The instability of liquid surfaces when accelerated in a direction perpendicular to their plane," Proc. R. Soc. London A **201**, 192–196 (1950).

[3] B.-I. Jun, T. W. Jones, and M. L. Norman, "Interaction of Rayleigh-Taylor fingers and circumstellar cloudlets in young supernova remnants," Astrophys. J. **468**, 59–63 (1996).

[4] C. C. Joggerst, A. Almgren, and S. E. Woosley, "Three-dimensional simulations of Rayleigh-Taylor mixing in core-collapse supernovae," Astrophys. J. **723**, 353–363 (2010).

[5] S. E. Bodner, "Rayleigh-Taylor instability and laser-pellet fusion," Phys. Rev. Lett. **33**, 761–764 (1974).

[6] J. D. Lindl and W. C. Mead, "Two-dimensional simulation of fluid instability in laser-fusion pellets," Phys. Rev. Lett. **34**, 1273–1276 (1975).

[7] J. Lindl, "Development of the indirect-drive approach to inertial confinement fusion and the target physcis basis for ignition and gain," Phys. Plasmas **2**, 3933–4024 (1995).

[8] W. W. Hsing, C. W. Barnes, J. B. Beck, N. M. Hoffman, D. Galmiche, A. Richard, J. Edwards, P. Graham, S. Rothman, and B. Thomas, "Rayleigh-Taylor instability evolution in ablatively driven cylindrical implosions," Phys. Plasmas **4**, 1832–1840 (1997).

[9] G. I. Bell, *Taylor instability on cylinders and spheres in small amplitude approximation*, Tech. Rep. LA-1321 (Los Alamos Scientific Laboratory, 1951).

[10] M. S. Plesset, "On the stability of fluid flows with spherical symmetry," J. Appl. Phys. **25**, 96–98 (1954).

[11] P. Amendt, J. D. Colvin, J. D. Ramshaw, H. F. Robey, and O. L. Landen, "Modified Bell-Plesset effect with compressibility: Application to double-shell ignition target designs," Phys. Plasmas **10**, 820–829 (2003).

[12] R. Epstein, "On the Bell-Plesset effects: The effects of uniform compression and geometrical convergence on the classical Rayleigh-Taylor instability," Phys. Plasmas **11**, 5114–5124 (2004).

[13] K. O. Mikaelian, "Rayleigh-Talor and Richtmyer-Meshkov instabilities and mixing in stratified cylindrical shells," Phys. Fluids **17**, 094105 (2005).

[14] V. A. Smalyuk, M. Barrios, J. A. Caggiano, D. T. Casey, C. J. Cerjan, D. S. Clark, M. J. Edwards, J. A. Frenje, M. Gatu-Johnson, V. Y. Glebov, G. Grim, S. W. Haan, B. A. Hammel, A. Hamza, D. E. Hoover, W. W. Hsing, O. Hurrican, J. D. Kilkenny, J. L . Kline, J. P. Knauer, J. Kroll, O. L. Landen, J. D. Lindl, T. Ma, J. M. McNaney, M. Mintz, A. Moore, A. Nikroo, T. Parham, J. L. Peterson, R. Petrasso, L. Pickworth, J. E. Pino, K. Raman, S. P. Regan, B. A. Remington, H. F. Robey, D. P. Rowley, D. B. Sayre, R. E. Tipton, S. V. Weber, K. Widmann, D. C. Wilson, and C. B. Yeamans, "Hydrodynamic instability growth and mix experiments at the National Ignition Facility," Phys. Plasmas **21**, 056301 (2014).

[15] V. A. Smalyuk, R. E. Tipton, J. E. Pino, D. T. Casey, G. P. Grim, B. A. Remintgon, D. P. Rowley, S. V. Weber, M Barrios, L. R. Benedetti, D. L. Bleuel, D. K. Bradley, J. A. Caggiano, D. A. Callahan, C. J. Cerjan, D. S. Clark, D. H. Edgell, M. J. Edwards, J. A. Frenje, M. Gatu-Johnson, V. Y. Glebov, S. Glenn, S. W. Haan, A. Hamza, R. Hatarik, W. W. Hsing, N. Izumi, S. Khan, J. D. Kilkenny, J. Kline, J. Knauer, O. L. Landen, T. Ma, J. M. McNaney, M. Mintz, A. Moore, A. Nikroo, A. Pak, T. Parham, R. Petrasso, D. B. Sayre, M. B. Schneider, R. Tommasini, R. P. Town, K. Widmann, D. C. Wilson, and C. B. Yeamans, "Measurements of an ablator-gas atomic mix in indirectly driven implosions at the National Ignition Facility," Phys. Rev. Lett. **112**, 025002 (2014).

[16] D. T. Casey, V. A. Smalyuk, R. E. Tipton, J. E. Pino, G. P. Grim, B. A. Remington, D. P. Rowley, S. V. Weber, M. Barrios, L. R. Benedetti, D. L. Bleuel, E. J. Bond, D. K. Bradley, J. A. Caggiano, D. A. Callahan, C. J. Cerjan, K. C. Chen, D. H. Edgell, M. J. Edwards, D. Fittinghoff, J. A. Frenje, M. Gatu-Johnson, V. Y. Glebov, S. Glenn, N. Guler, S. W. Haan, A. Hamza, R. Hatarik, H. W. Herrmann, D. Hoover, W. W. Hsing, N. Izumi, P. Kervin, S. Khan, J. D. Kilkenny, J. Kline, J. Knauer, G. Kyrala, O. L. Landen, T. Ma, A. G. MacPhee, J. M. McNaney, M. Mintz, A. Moore, A. Nikroo, A. Pak, T. Parham, R. Petrasso, H. G. Rinderknecht, D. B. Sayre, M. Schneider, W. Stoeffl, R. Tommasini, R. P. Town, K. Widmann, D. C. Wilson, and C. B. Yeamans, "Development of the CD Symcap platform to study gas-shell mix in implosions at the National Ignition Facility," Phys. Plasmas **21**, 092705 (2014).

[17] P. Amendt, J. D. Colvin, R. E. Tipton, D. E. Hinkel, M. J. Edwards, O. L. Landen, J. D. Ramshaw, L. J. Suter, W. S. Varnum, and R. G. Watt, "Indirect-drive noncryogenic double-shell ignition targets for the National Ignition Facility: Design and analysis," Phys. Plasmas **9**, 2221–2233 (2002).

[18] P. A. Bradley, J. A. Cobble, I. L. Tregillis, M. J. Schmitt, K. D. Obrey, V. Glebov, S. H. Batha, G. R. Magelssen, J. R. Fincke, S. C. Hsu, N. S. Krasheninnikova, T. J. Murphy, and F. J. Wysocki, "Role of shocks and mix caused by capsule defects," Phys. Plasmas **19**, 092703 (2012).

[19] P. A. Bradley, "The effect of mix on capsule yields as a function of shell thickness and gas fill," Phys. Plasmas **21**, 062703 (2014).

[20] S. V. Weber, D. T. Casey, D. C. Eder, J. D. Kilkenny, J. E. Pino, V. A. Smalyuk, G. P. Grim, B. A. Remington, D. P. Rowley, C. B. Yeamans, R. E. Tipton, M. Barrios, R. Benedetti, L. Berzak Hopkins, D. L. Bleuel, E. J. Bond, D. K. Bradley, J. A. Caggiano, D. A. Callahan, C. J. Cerjan, D. S. Clark, L. Divol, D. H. Edgell, M. J. Edwards, M. J. Eckart, D. Fittinghoff, J. A. Frenje, M. Gatu-Johnson, V. Y. Glebov, S. Glenn, N. Guler, S. W. Haan, A. Hamza, R. Hatarik, H. Herrmann, D. Hoover, W. W. Hsing, N. Izumi, O. S. Jones, M. Kervin, S. Khan, J. Kline, J. Knauer, A. Kritcher, G. Kyrala, O. L. Landen, S. Le Pape, T. Ma, A. J. Mackinnon, A. G. MacPhee, M. M. Marinak, J. M. Mcnaney, N. B. Meezan, F. E. Merrill, M. Mintz, A. Moore, D. H. Munro, A. Nikroo, A. Pak, T. Parham, R. Petrasso, H. G. Rinderknecht, D. B. Sayre, S. M. Sepke, B. K. Spears, W. Stoeffl, R. Tommasini, R. P. Town, P. Vole-

gov, K. Widmann, D. C. Wilson, and A. B. Zylstra, "Simulations of indirectly driven gas-filled capsules at the National Ignition Facility," Phys. Plasmas **21**, 112706 (2014).

[21] G. Dimonte and R. Tipton, "K-L turulence model for the self-similar growth of the Rayleigh-Taylor and Richtmyer-Meshkov instabilities," Phys. Fluids **18**, 085101 (2006).

[22] B. E. Morgan and M. E. Wickett, "Three-equation model for the self-similar growth of Rayleigh-Taylor and Richtmyer-Meshkov instabilities," Phys. Rev. E **91**, 043002 (2015).

[23] B. E. Morgan, O. Schilling, and T. A. Hartland, "Two-length-scale turbulence model for self-similar buoyancy-, shock-, and shear-driven mixing," Phys. Rev. E **97**, 013104 (2018).

[24] D. Besnard, F. H. Harlow, and R. Rauenzahn, *Conservation and Transport Properties of Turbulence with Large Density Variations*, Tech. Rep. LA-10911-MS (Los Alamos National Laboratory, 1987).

[25] D. C. Besnard, F. H. Harlow, R. M. Rauenzahn, and C. Zemach, *Turbulence transport equations for variable-density turbulence and their relationship to two-field models*, Tech. Rep. LAUR-12303 (Los Alamos National Laboratory, 1992).

[26] A. Banerjee, R. A. Gore, and M. J. Andrews, "Development and validation of a turbulent-mix model for variable-density and compressible flows," Phys. Rev. E **82**, 046309 (2010).

[27] J. D. Schwarzkopf, D. Livescu, J. R. Baltzer, R. A. Gore, and J. R. Ristorcelli, "A two-length scale turbulence model for single-phase multi-fluid mixing," Flow Turbul. Combust. **96**, 1–43 (2016).

[28] J. R. Ristorcelli, "Exact statistical results for binary mixing and reaction in variable density turbulence," Phys. Fluids **29**, 020705 (2017).

[29] H. Sakagami and K. Nishihara, "Three-dimensional Rayleigh-Taylor instability of spherical systems," Phys. Rev. Lett. **65**, 432–435 (1990).

[30] D. L. Youngs and R. J. R. Williams, "Turbulent mixing in spherical implosions," Intl. J. Numer. Meth. Fluids **56**, 1597–1603 (2008).

[31] M. Lombardini and D. I. Pullin, "Small-amplitude perturbations in the three-dimensional cylindrical Richtmyer-Meshkov instability," Phys. Fluids **21**, 114103 (2009).

[32] M. Lombardini, D. I. Pullin, and D. I. Meiron, "Turbulent mixing driven by spherical implosions. Part 1. Flow description and mixing-layer growth," J. Fluid Mech. **748**, 85–112 (2014).

[33] M. Lombardini, D. I. Pullin, and D. I. Meiron, "Turbulent mixing driven by spherical implosions. Part 2. Turbulence statistics," J. Fluid Mech. **748**, 113–142 (2014).

[34] V. A. Thomas and R. J. Kares, "Drive asymmetry and the origin of turbulence in an ICF implosion," Phys. Rev. Lett. **109**, 075004 (2012).

[35] D. S. Clark, D. E. Hinkel, D. C. Eder, O. S. Jones, S. W. Haan, B. A. Hammel, M. M. Marinak, J. L. Milovich, H. F. Robey, L. J. Suter, and R. P. J. Town, "Detailed implosion modeling of deuterium-tritium layered experiments on the National Ignition Facility," Phys. Plasmas **20**, 056318 (2013).

[36] C. R. Weber, D. S. Clark, A. W. Cook, L. E. Busby, and H. F. Robey, "Inhibition of turbulence in inertial-confinement-fusion hot spots by viscous dissipation," Phys. Rev. E **89**, 053106 (2014).

[37] C. R. Weber, D. S. Clark, A. W. Cook, D. C. Eder, S. W. Haan, B. A. Hammel, D. E. Hinkel, O. S. Jones, M. M. Marinak, J. L. Milovich, P. K. Patel, H. F. Robey, J. D. Salmonson, S. M. Sepke, and C. A. Thomas, "Three-dimensional hydrodynamics of the deceleration stage in inertial confinement fusion," Phys. Plasmas **22**, 032702 (2015).

[38] D. S. Clark, C. R. Weber, J. L. Milovich, J. D. Salmonson, A. L. Kritcher, S. W. Haan, B. A. Hammel, D. E. Hinkel, O. A. Hurricane, O. S. Jones, M. M. Marinak, P. K. Patel, H. F. Robey, S. M. Sepke, and M. J. Edwards, "Three-dimensional simulatiosn of low foot and high foot implosion experiments on the National Ignition Facility," Phys. Plasmas **23**, 056302 (2016).

[39] B. M. Haines, G. P. Grim, J. R. Fincke, R. C. Shah, C. J. Forrest, K. Silverstein, F. J. Marshall, M. Boswell, M. M. Fowler, R. A. Gore, A. C. Hayes-Sterbenz, G. Jungman, A. Klein, R. S. Rundberg, M. J. Steinkamp, and J. B. Wilhelmy, "Detailed high-resolution three-dimensional simulations of OMEGA separated reactants inertial confinement fusion experiments," Phys. Plasmas **23**, 072709 (2016).

[40] B. E. Morgan, B. J. Olson, J. E. White, and J. A. McFarland, "Self-similarity of a Rayleigh-Taylor mixing layer at low Atwood number with a multimode initial perturbation," J. Turbul. **18**, 973–999 (2017).

[41] A. W. Cook, W. Cabot, and P. L. Miller, "The mixing transition in Rayleigh-Taylor instability," J. Fluid Mech. **511**, 333–362 (2004).

[42] W. H. Cabot and A. W. Cook, "Reynolds number effects on Rayleigh-Taylor instability with possible implications for type Ia supernovae," Nature Phys. **2**, 562–568 (2006).

[43] B. J. Olson and A. W. Cook, "Rayleigh-Taylor shock waves," Phys. Fluids **19**, 128108 (2007).

[44] B. J. Olson, J. Larsson, S. K. Lele, and A. W. Cook, "Non-linear effects of the combined Rayleigh-Taylor/Kelvin-Helmholtz instabilitiy," Phys. Fluids **23**, 114107 (2011).

[45] V. K. Tritschler, B. J. Olson, S. K. Lele, S. Hickel, X. Y. Hu, and N. A. Adams, "On the Richtmyer-Meshkov instability evolving from a deterministic multimode planar interface," J. Fluid Mech. **755**, 429–462 (2014).

[46] B. J. Olson and J. Greenough, "Large eddy simulation requirements for the Richtmyer-Meshkov instability," Phys. Fluid **26**, 044103 (2014).

[47] B. J. Olson and J. Greenough, "Comparison of two- and three-dimensional simulations of miscible rychtmyer-meshkov instability with multimode initial conditions," Phys. Fluid **26**, 101702 (2014).

[48] A. W. Cook, "Artificial fluid properties for large-eddy simulation of compressible turbulent mixing," Phys. Fluids **19**, 055103 (2007).

[49] A. W. Cook, "Enthalpy diffusion in multicomponent flows," Phys. Fluids **21**, 055109 (2009).

[50] R.W. Sharp and R.T. Barton, *HEMP advection model*, Report UCID 17809 (Lawrence Livermore Laboratory, Livermore, CA, 1981).

[51] R.M. Darlington, T.L. McAbee, and G. Rodrigue, "A study of ALE simulations of Rayleigh-Taylor instability," Computer Physics Communications **135**, 58–73 (2001).

[52] Tz.V. Kolev and R.N. Rieben, "A tensor artificial viscosity using a finite element approach," J. Comput. Phys.

228, 8336–8366 (2009).

[53] M.J. Berger and J. Oliger, "Adaptive mesh refinement for hyperbolic partial differential equations," J. Comput. Phys. **53**, 484–512 (1984).

[54] M.J. Berger and P. Colella, "Local adaptive mesh refinement for shock hydrodynamics," J. Comput. Phys. **82**, 64–84 (1989).

[55] B. E. Morgan J. A. Greenough, "Large-eddy and unsteady RANS simulations of a shock-accelerated heavy gas cylinder," Shock Waves **26**, 355–383 (2016).

[56] K. S. Raman, O. A. Hurrican, H.-S. Park, B. A. Remington, H. Robey, V. A. Smalyuk, R. P. Drake, C. M. Krauland, C. c. Kuranz, J. F. Hansen, and E. C. Harding, "Three-dimensional modeling and analysis of a high energy density Kelvin-Helmholtz experiment," Phys. Plasmas **19**, 092112 (2009).

[57] S. F. Khan, S. A. MacLaren, J. D. Salmonson, T. Ma, G. A. Kyrala, J. E. Pino, J. R. Rygg, J. E. Field, R. Tommasini, J. E. Ralph, D. P. Turbull, A. J. Kackinnon, K. L. Baker, L. R. Benedetti, D. K. Bradley, P. M. Celliers, E. L. Dewald, T. R. Dittrich, L. Berzak Hopkins, N. Izumi, M. L. Kervin, J. L. Kline, S. R. Nagel, A. Pak, and R. E. Tipton, "Symmetry tuning of a near one-dimensional 2-shock platform for code validation at the National Ignition Facility," Phys. Plasmas **23**, 042708 (2016).

[58] M. Gatu Johnson, A. B. Zylstra, A. Bacher, C. R. Brune, D. T. Casey, C. Forrest, H. W. Hermann, M. Hohenberger, D. B. Sayre, R. M. Bionta, J.-L. Bourgade, J. A. Caggiano, C. Cerjan, R. S. Craxton, D. Dearborn, M. Farrell, J. A. Frenje, E. M. Garcia, V. Yu. Glebov, G. Hale, E. P. Hartouni, R. Hatarik, M. Hohensee, D. M. Holunga, M. Hoppe, R. Janezic, S. F. Khan, J. D. Kilkenny, Y. H. Kim, J. P. Knauer, T. R. Kohut, B. Lahmann, O. Landoas, C. K. Li, F. J. Marshall, L. Masse, A. McEvoy, P. McKenty, D. P. McNabb, A. Nikroo, T. G. Parham, M. Paris, R. D. Petrasso, J. Pino, P. B. Radha, B. Remington, H. G. Rinderknecht, H. Robey, M. J. Rosenberg, B. Rosse, M. Rubery, T. C. Sangster, J. Sanchez, M. Schmitt, M. Schoff, F. H. Séguin, W. Seka, H. Sio, C. Stoeckl, and R. E. Tipton, "Development of an inertial confinement fusion platform to study charged-particle-producing nuclear reactions relevant to nuclar astrophysics," Phys. Plasmas **24**, 041407 (2017).

[59] M. Gatu Johnson, D. T. Casey, M. Hohenberger, A. B. Zylstra, A. Bacher, C. R. Brune, R. M. Bionta, R. S. Craxton, C. L. Ellison, M. Farrell, J. A. Frenje, W. Garbett, E. M. Garcia, G. P. Grim, E. Hartouni, R. Hatarik, H. W. Herrmann, M. Hohensee, D. M. Holunga, M. Hoppe, M. Jackson, N. Kabaldi, S. F. Khan, J. D. Kilkenny, T. R. Kohut, B. Lahmann, H. P. Le, C. K.

Li, L. Masse, P. W. McKenty, D. P. McNabb, A. Nikroo, T. G. Parham, C. E. Parker, R. D. Petrasso, J. Pino, B. Remington, N. G. Rice, H. G. Rinderknecht, M. J. Rosenberg, J. Sanchez, D. B. Sayre, M. E. Schoff, C. M. Shuldberg, F. H. Séguin, H. Sio, Z. B. Walters, and H. D. Whitley, "Optimization of a high-yield, low-areal-density fusion product source at the National Ignition Facility with applications in nucleosynthesis experiments," Phys. Plasmas **25**, 056303 (2018).

[60] S. I. Warshaw, *The TDF system for thermonuclear plasma reaction rates, mean energies and two-body final state particle spectra*, Report UCRL-ID-144510 (Lawrence Livermore National Laboratory, Livermore, CA, 2001).

[61] E. G. Corman, W. E. Loewe, G. E. Cooper, and A. M. Winslow, "Multigroup diffusion of energetic particles," Nucl. Fusion **15**, 377–386 (1975).

[62] H. Brysk, "Electron-ion equilibration in a partially degenerate plasma," Plasma Phys. **16**, 927–932 (1974).

[63] D. C. Wilcox, *Turbulence Modeling for CFD* (DCW Industries, La Cañada, California, 2006).

[64] O. Schilling and N. J. Mueschke, "Turbulent transport and mixing in transitional Rayleigh-Taylor unstable flow: *A priori* assessment of gradient-diffusion and similarity modeling," Phys. Rev. E **96**, 063111 (2017).

[65] G. W. Sutton, "Decay of passive scalar fluctuations in isotropic homogeneous turbulence," Phys. Fluids **11**, 671 (1968).

[66] G. Dimonte and M. Schneider, "Density ratio dependence of Rayleigh-Taylor mixing for sustained and impulsive acceleration histories," Phys. Fluids **12**, 304–321 (2000).

[67] G. Dimonte, D. L. Youngs, A. Dimits, S. Weber, M. Marinak, S. Wunsch, C. Garasi, A. Robinson, M. J. Andrews, P. Ramaprabhu, A. C. Calder, B. Fryxell, J. Biello, L. Dursi, P. MacNeice, K. Olson, P. Ricker, R. Rosner, F. Timmes, H. Tufo, Y.-N. Young, and M. Zingale, "A comparative study of the turbulent Rayleigh-Taylor instability using high-resolution three-dimensional numerical simulations: The Alpha-Group collaboration," Phys. Fluids **16**, 1668–1693 (2004).

[68] P. Ramaprabhu and M. J. Andrews, "Experimental investigation of Rayleigh-Taylor mixing at small Atwood numbers," J. Fluid Mech. **502**, 233–271 (2004).

[69] R. M. More, K. H. Warren, D. A. Young, and G. B. Zimmerman, "A new quotidian equation of state (QEOS) for hot dense matter," Phys. Fluids **31**, 3059–3078 (1988).

[70] D. A. Young and E. M. Corey, "A new global equation of state model for hot, dense matter," J. Appl. Phys. **78**, 3748–3755 (1995).

[71] J. R. Ristorcelli and T. T. Clark, "Rayleigh-Taylor turbulence: self-similar analysis and direct numerical simulations," J. Fluid Mech. **507**, 213–253 (2004).